# Environmental magnetic fingerprinting of anthropogenic and natural atmospheric deposition over southwestern Europe

Juan C. Larrasoaña[a,*], Jorge Pey[b,c], Xiang Zhao[d], David Heslop[d], Tania Mochales[a], Pilar Mata[e], Elisabet Beamud[f], Jesús Reyes[e], José C. Cerro[g], Noemí Pérez[h], and Sonia Castillo[i,j]

[a] Instituto Geológico y Minero de España, C/Manuel Lasala 44, 50006, Zaragoza, Spain
[b] Aragonese Foundation for Research & Development – ARAID, Av. de Ranillas 1-D, 50018 Zaragoza, Spain
[c] Instituto Pirenaico de Ecología, CSIC, Av. Montañana 1005, 50059 Zaragoza, Spain
[d] Research School of Earth Sciences, The Australian National University, Canberra, ACT 2601, Australia
[e] Instituto Geológico y Minero de España, C/La Calera 1, 28760 Tres Cantos, Spain
[f] Paleomagnetic Laboratory CCiTUB-Geo3Bcn, Geosciences Barcelona, CSIC, 08028 Barcelona, Spain
[g] Universitat Illes Balears, Carretera de Valldemossa km7.4, 07122, Palma, Spain
[h] Instituto de Diagnóstico Ambiental y Estudios del Agua, CSIC, C/Jordi Girona 18-26, 08028 Barcelona, Spain
[i] Andalusian Institute for Earth System Research (IISTA-CEAMA), Universidad de Granada, Av. del Mediterráneo, 18071 Granada, Spain
[j] Department of Applied Physics, Universidad de Granada, Av. de la Fuente Nueva, 18071 Granada, Spain

[*] Corresponding author
E-mail: jc.larra@igme.es

**Abstract**

Here we present an environmental magnetic study of atmospheric deposition collected by a multi-site network in Spain that covers fourteen locations representative of urban, industrial, agricultural, and natural environments across southwestern Europe. We have combined magnetic methods with scanning electron microscopy and geochemical data to characterize the magnetic mineral assemblages of particular matter across different types of sites and phenomenological scenarios, and to unravel their environmental significance in terms of the most important anthropogenic and natural components of atmospheric

deposition. Our results enable identification of two magnetite/maghemite components of anthropogenic origin, derived mostly from vehicular traffic, plus a hematite component associated with a baseline supply of north African dust, in all the studied sites regardless of their type. The ubiquitous presence of anthropogenic magnetite/maghemite particles in pristine natural environments, albeit in lower concentrations, point to their arrival from neighbouring urban areas through atmospheric mixing processes. Samples including particulate matter deposited during distinctively intense periods of north African dust supply are characterized by a fourth component, represented also by coarser-grained hematite, that is likely derived from a different source area within the Sahara Desert. The concomitant increase observed in these cases in the amounts of magnetite/maghemite particles suggests strongly that part of the magnetite/maghemite load attributed to anthropogenic sources for the rest of the phenomenological scenarios is aeolian in origin. This seems to explain the overall moderate correlation observed between magnetite/maghemite contents and proxies for vehicular traffic, and demonstrates the need for caution when interpreting environmental magnetic proxies for magnetite/maghemite abundances in terms of anthropogenic loads. This is especially the case in southern European cities where a steady supply of north African dust occurs throughout most of the year. Our results show a good correlation between hematite abundances and geochemical proxies for north African dust, which collectively delineate broad maxima during the summer and large peaks during distinctive dust breakouts. Thus, environmental magnetic proxies of hematite abundances can be used to monitor the contribution of natural sources to atmospheric deposition.

**Key words:** Atmospheric deposition, particulate matter, environmental magnetism, pollution, north African dust, Spain.

## 1. Introduction

Rock magnetic methods provide a rapid, cost-effective and non-destructive means of identifying magnetic mineral particles and quantifying their concentration in a wide variety of materials, including atmospheric particulate matter (PM) (Verosub and Roberts, 1995; Petrovský and Ellwood, 1999; Evans and Heller, 2003; Liu et al., 2012). Most PM-producing anthropogenic activities, such as burning of fossil fuels (car, shipping and power-plant emissions), industrial processes involving high-temperature treatments (e.g., steel, cement and ceramic production), or abrasion of metallic (e.g., brakes) and iron-bearing (e.g., tyres) vehicular parts, are invariably associated with the

production of magnetic particles (Petrovský and Ellwood, 1999; Evans and Heller, 2003; Liu et al., 2012; Hofman et al., 2017). The low-coercivity minerals magnetite ($Fe_3O_4$) and maghemite ($\gamma$–$Fe_2O_3$) are, by far, the most commonly reported magnetic minerals in anthropogenic PM (Muxworthy et al., 2002, 2003; Spassov et al., 2004; Sagnotti et al., 2006, 2009; Saragnese et al., 2011; Sagnotti and Winkler, 2012; Revuelta et al., 2014, Maher et al., 2016; Hofman et al., 2017). These minerals have similar magnetic properties and are typically reported as magnetite/maghemite or magnetite-like assemblages unless more diagnostic magnetic measurements are made (Muxworthy et al., 2002). The high-coercivity mineral hematite ($\alpha$–$Fe_2O_3$) is also formed in industrial (e.g., steel manufacturing) and power-plant fly-ashes (Petrovský and Ellwood, 1999), but has been reported less frequently in anthropogenic PM. The weak spontaneous magnetization of hematite means that in mixed magnetic mineral assemblages its diagnostic signatures are often overwhelmed by the signals of more strongly magnetic magnetite-maghemite components (Saragnese et al., 2011, Hofman et al., 2017; Tan et al., 2018). Combined magnetic and scanning/transmission electron microscopy (SEM, TEM) observations indicate that anthropogenic magnetite and maghemite are typically found as isolated particles, spherules and irregular aggregates. These individual particles range in size from <20 nm in the so-called superparamagnetic (SP) grains, from 20 to 100 nm in stable single domain (SD), from 100 to 300 nm in pseudo-single domain (PSD) or vortex, to >300 nm in multi-domain (MD) particles (Sagnotti et al., 2009, Saragnese et al., 2011; Hofman et al., 2017; Tan et al., 2018). Anthropogenic hematite is often reported as SP to MD platy specularite of lamellar crystal (Petrovský and Ellwood, 1999), which range in size between a few nanometres and some tens of microns. Because of their grain size, magnetic particles are inherently linked to respirable anthropogenic PM (e.g., defined as PM with an aerodynamic diameter of ≤10 μm, $PM_{10}$), thereby posing one of the biggest environmental concerns in urban areas (WHO, 2006; Maher et al., 2016). The ability of rock magnetic measurements to rapidly identify and quantify harmful atmospheric particles via their association with magnetic particles has led to widespread use of environmental magnetic techniques in PM studies over the last two decades (see Evans and Heller, 2003; Liu et al., 2012; Hofman et al., 2017).

Most studies have concentrated on samples obtained in air-quality stations, where $PM_{10}$ (and sometimes also $PM_{2.5}$) is collected actively by pumping air through appropriate filters (e.g., Muxworthy et al., 2001, 2003; Spassov et al., 2004; Sagnotti et al., 2006; Saragnese et al., 2011; Revuelta et al., 2014), or on biomaterials such as tree leaves, bark or mosses, were PM accumulates by passive fallout with no grain-size bias (Matzka and

Maher, 1999; Sagnotti et al., 2009; Sagnotti and Winkler, 2012; Hofman et al., 2017). Fewer studies have been based on direct collection of street dust (Tan et al., 2018), on PM accumulated in passive collectors designed to avoid grain-size biases (Muxworthy et al., 2002; Cao et al., 2015), or on PM accumulated in a combination of media (Abbasi et al., 2020). Although these studies often include material collected from rural sites regarded as the regional natural background (Spassov et al., 2003; Saragnese et al., 2011; Sagnotti et al., 2006), they typically focus on urban and industrial areas so that anthropogenic PM is sampled. MD and SP magnetite/maghemite grains are the most abundant magnetic particles reported in anthropogenic PM (Sagnotti et al., 2006, 2009; Lehndorff et al., 2006; Saragnese et al., 2011; Hofman et al., 2017), and a number of studies suggest that coarse MD magnetite grains with an outer layer of SP maghemite particles are representative of anthropogenic PM across a large number of urban and industrial areas (Muxworthy et al., 2003; Sagnotti et al., 2009; Saragnese et al., 2011; Revuelta et al., 2014). Such particles appear to derive from a magnetite precursor, formed by combustion or frictional heating processes, whose outer core has been oxidised to maghemite during subsequent cooling and atmospheric ageing (Muxworthy et al., 2003; Saragnese et al., 2011; Revuelta et al., 2014). A high-coercivity mineral, likely hematite, has been reported in urban and industrial PM (Saragnese et al., 2011; Revuelta et al., 2014), yet its origin and environmental significance has been seldom addressed due to difficulties in discerning its origin. Sampling duration also varies between different studies of anthropogenic PM, ranging from 24 hours for some studies of PM collected in air-quality stations (Spassov et al., 2004; Sagnotti et al., 2006) to 1 year in some studies dealing with PM accumulated in self-designed collectors (Cao et al., 2015), with sampling intervals ranging between 6 days and a full growing season when biological material is used (Hofman et al., 2017). Monitoring periods also differ, with lengths varying between some months and one year (Saragnese et al., 2011; Sagnotti et al., 2006). One of the prime goals of studies dealing with urban and industrial PM has been the development of magnetic parameters that can be employed, supported by additional geochemical data, as proxies for anthropogenic pollution load (see Hofman et al., 2017).

In comparison to anthropogenic PM, the magnetic characterization of natural PM has received very little attention. Locally-derived dust is expected to be relevant only in drylands (Abbasi et al., 2020) or agricultural regions or where the soil is, at least, temporally exposed. In contrast, desert dust sourced from north Africa (NAD) is known to be a substantial component of PM across many European regions, especially around the Mediterranean Sea (Pey et al., 2013, Varga et al., 2014). NAD contains large amounts

of magnetite, maghemite, hematite and goethite spanning a wide grain-size range (Larrasoaña et al., 2015). It is, therefore, surprising that magnetite/maghemite grains derived from NAD have been reported only in a limited number of urban areas (Spassov et al., 2004; Sagnotti et al., 2006; Revuelta et al., 2014), possibly because it is obscured commonly by anthropogenic magnetite. Equally surprising is the lack of studies in which hematite has been reported as a constituent of natural PM (Sagnotti et al., 2006). Given the abundance of magnetic minerals in NAD, it is very likely that at least part of the magnetite/maghemite and hematite reported in urban and industrial PM actually has an aeolian origin. Yet, compelling evidence for this is still to be provided, and the implications for developing magnetic proxies for pollution remain unexplored. Although the knowledge gained from the magnetic characterization of PM has increased tremendously over the last decades, the large variety of methods, sampling times, and temporal and spatial resolutions employed have made it challenging to develop a comprehensive understanding of underlying anthropogenic and natural processes responsible for accumulation of PM at large temporal and geographical scales.

The DONAIRE network was designed to carry out an integrated study of atmospheric deposition across a large area of Spain that includes the Cantabrian-Pyrenean area, the Ebro basin, and the Mediterranean region (Pey et al., 2020). This area is characterized by variable climatic conditions that, combined with a complex topography (heights ranging from sea-level to over 3000 m a.s.l.) provide a wide variety of environmental conditions. Land-use is also highly variable, and includes a mixture of densely populated urban areas, industrial hot-spots, quasi-demographic deserts, agricultural regions, and pristine natural areas. Here we present an environmental magnetic study of atmospheric deposition collected in the framework of the DONAIRE network, which includes 14 representing urban, industrial, agricultural and natural areas, between June 2016 and June 2017. We have performed detailed magnetic characterization of the PM, assisted by SEM observations, across a set of samples selected to be representative for the different areas and phenomenological scenarios of atmospheric deposition. This information has been combined with bulk environmental magnetic properties and selected geochemical data for the entire set of samples. By integrating all results, the significance of bulk environmental magnetic properties in terms of the most important anthropogenic and natural components of atmospheric deposition, and their temporal variations, has been determined for an area representative of different anthropized and natural settings in SW Europe. The forthcoming completion of the full geochemical dataset will enable a detailed source apportionment of the atmospheric deposition collected in the framework

of the DONAIRE network, constraining the reliability of the magnetic proxies considered in this contribution.

## 2. Materials and methods

### 2.1. Sites, samples, and atmospheric deposition scenarios

Samples were collected using home-produced collectors consisting of a plastic funnel (with a diameter ranging from 26 to 34 cm) that acts as the collecting surface, a 10L plastic container, and a silicone tube that connects the funnel with the container. The silicone tube is mounted inside a rigid PVC tube that, along with the plastic container, is placed within a dark box to keep the samples in opaque conditions. Eight of the collectors were placed in the roof of air quality monitoring sites or other buildings (Fig. 1). The remaining collectors were placed at least 2 m above the ground in order to minimize the impact of local resuspension. A total of 14 contrasting micro-environments form our monitoring network, which includes four urban areas of variable sizes with their accompanying peripheral industrial activity (Pamplona, Zaragoza, Barcelona, and Palma), a heavily-polluted industrial town (Monzón), two agricultural territories (Ejea de los Caballeros and Almudévar), and seven pristine natural environments that serve as regional backgrounds (Enol, Orgi, Ordesa, Chiprana, Montseny, Joan March and Frigiliana) (Fig. 1, Table 1). Samples were collected every second week throughout the whole survey, which started at the beginning of June 2016 (when the collectors were deployed) and lasted till the end of June 2017 (when maintenance and sampling of the collectors could not be extended for a number of sites). Exceptions to this are the sites of Enol (ENO, background site), Ejea de los Caballeros (EDC, agricultural site) and Frigiliana (FRI, background site); ENO was sampled every two months due to logistic constraints, EDC was removed in March 2017 after being vandalized twice, and FRI was only incorporated to the network in October 2016. Although a 1-year monitoring period might not be representative of the climatology of the studied areas, it enables robust magnetic characterization of atmospheric deposition throughout a large region of SW Europe and a reliable assessment of their fluctuations as a function of seasonal variations and underlying sources. Details on the location, type and monitoring period for the sites considered in this study can be found in Table 1 and in Pey et al. (2020).

Sample collection involved: 1) cleaning of the funnel using 500 ml of bi-distilled water and a plastic brush, so that the resulting solution was combined with any material that had accumulated in the container either in the form of dry (free fall) or wet (washed out by rainfall) deposition; and 2) the replacement of the containers by new ones. Once in the

laboratory, samples were stored in dark conditions at 4ºC before filtering, which involved two steps. The first filtering step employed a 100 μm mesh to remove biological particles (mostly insect and plant fragments). The second filtering employed 47 μm-diameter quartz fibre filters (PALL tissuquarzt 2500QAT-UP), which had been previously kept in controlled conditions (Tª 22-24 ºC; RH 25-35%) and weighed two times on different days. For each sample, between two and six sister filters were obtained depending on the amount of material collected (FRI-3.1 would indicate the first filter from sample 3 collected in Frigiliana). The filtered water was subjected to chemical analyses to provide information concerning the soluble fraction of atmospheric deposition (Pey et al., 2020), which is not considered here. After drying at room temperature, each filter was weighed two times on different days. The insoluble PM collected by the filters, is the subject of the environmental magnetic analyses presented here.

Atmospheric deposition across the study area occurs under seasonally contrasting meteorological scenarios (Pey et al., 2013, 2020; Revuelta et al., 2014). The winter is characterized by either the advection of W and NW Atlantic low-pressure systems that bring rainfall, or by anticyclonic conditions with negligible precipitation. The spring and fall are dominated by highly dynamic atmospheric conditions associated to the arrival of both Atlantic and Mediterranean depressions. This situation contrasts with that prevailing during summer, when recirculation and mixing of local air masses, and the arrival of north African warm winds, dominate. The passage of Atlantic and Mediterranean depressions during the fall, winter and spring drive episodes dominated by wet deposition that often involve the transport of locally-produced particles away from their source. Atlantic depressions are sometimes associated with the arrival of southerly winds sourced in north Africa, a situation that is accompanied by high NAD loads that are washed out by rain mainly over the eastern half of the Iberian Peninsula and the Western Mediterranean basin. The most prominent NAD outbreaks reported during the monitoring period of the DONAIRE network occurred in November 2016 and February 2017, and affected most of the studied sites to variable extents (see Pey et al., 2020 and http://www.bsc.es/projects/earthscience/visor/dust/med8/dep/archive/). In contrast, winter anticyclonic conditions, cause nearly stagnant conditions throughout much of the studied area (Pey et al., 2020; Revuelta et al., 2014). Atmospheric dispersion is then limited, and locally-derived particles constitute the bulk of the then dominant dry deposition. One such long anticyclonic period occurred during December 2016 and the first two weeks of January 2017. Dry deposition also dominates over the summer, but the recirculation of local air masses results in mixing and redistribution of atmospheric

particles with different origins. Penetration of north African air masses also results in regular delivery of dust particles throughout the warm season, which accumulate mainly as dry deposition following a north-south decreasing gradient across the Iberian Peninsula (e.g., Pey et al., 2013). On some particular occasions during the summer (e.g., August 2016), the advection of north African air masses can reach a considerable magnitude and result in the accumulation of significantly higher amounts of desert dust. All the aforementioned meteorological scenarios typically last between a few days and some weeks, and their signature is prone to be mixed at the studied sites given the biweekly sampling.

## 2.2. Rock magnetic characterization

Samples representative for all types of studied sites and atmospheric deposition scenarios were selected for detailed rock magnetic measurements, which were conducted with a Princeton Measurements Corporation vibrating sample magnetometer at the Black Mountain Paleomagnetic Laboratory of the Australian National University. Isothermal remanent magnetisation (IRM) acquisition curves were measured at more than 50 steps, approximately equally spaced on a logarithmic scale, from 1 mT up to 1 T (Kruiver et al., 2001). IRM curves were unmixed using the MAX UnMix web application (Maxbauer et al., 2016) to determine the main magnetic minerals contributing to the IRM. Hysteresis loops were measured with a maximum field of 1 T, after which a backfield magnetization was applied in a succession of fields of up to 1 T. Hysteresis parameters $M_s$ (saturation magnetisation), $M_{rs}$ (saturation remanent magnetisation), $H_c$ (coercivity) and $H_{cr}$ (coercivity of remanence) were used to plot the results in the Day diagram (Day et al., 1977), which provides a rough inference on the magnetic domain state (and hence grain size) of the studied magnetic assemblages (Roberts et al., 2018). Due to the limited amount of material present in the filters, reliable IRM acquisition curves and hysteresis data could be only obtained with measurement averaging times greater than 10 s. Reliable results could not, however, be obtained for samples with the lowest atmospheric deposition loads, which correspond to background sites without prominent NAD contributions. A subset of samples, representative of the most relevant types of sites and deposition scenarios, were selected for measurement of irregular first order reversal curve (FORC) distributions (Zhao et al., 2015) following the approach of Zhao et al. (2017), which enables distinction of different domain state signatures.

## 2.3. SEM observations

Samples representative for all types of studied sites and atmospheric deposition scenarios were selected for the electron microscopy study to determine type, size and shape of particulate matter deposited on each filter. The observations have been carried out on small pieces (10 x 0.5 mm) taken from the central part of sister filters. The filters were placed with conductive adhesive over Al-stubs and coated with a Cressington 208 carbon coater. Analyses were performed with a JSM-6010PLUS/LA InTouchScope™ scanning electron microscope at IGME. The observation conditions involve high vacuum, 20 kv, and 10 mm of working distance (WD). Most of the images have been taken with the backscattered electron detector to better estimate compositional variations of the particles of interest. Energy dispersive analysis (EDX) was performed on individual particles to obtain qualitative compositions.

## 2.4. Bulk environmental magnetic measurements

Bulk magnetic properties were measured, after folding and placing one sister filter for each sample in standard paleomagnetic boxes, at the Paleomagnetic Laboratory of the Institute Geosciences Barcelona (CCiTUB-CSIC), Spain. The magnetic susceptibility was measured with a KLY-2 magnetic susceptibility bridge with a field of 0.1 mT at a frequency of 470 Hz. The data provided represent the average of three measurements for each filter. Initial attempts to measure frequency-dependence of magnetic susceptibility (using a Bartington Instruments MS3 susceptibility meter coupled to a MS2B sensor) yielded unreliable results due to the very small amount of material accumulated on the filters (typically < 50 mg, Pey et al., 2020). We then measured two IRMs applied with an IRM10-30 pulse magnetizer (ASC Scientific) at fields of 0.3 and 1.2 T (IRM@0.3T and IRM@1.2T), which were measured using a 2G Enterprises SRM755 superconducting rock magnetometer. Due to technical problems, the anhysteretic remanent magnetisation (ARM) could not be measured prior to IRM analyses. A set of 5 blank samples was prepared with empty filters to measure their magnetic susceptibility, IRM@0.3T and IRM@1.2T. The average of these measurements was subtracted from the measured magnetic properties of all samples to account for the combined signal of the quartz filter and the paleomagnetic boxes, whose magnetic moment is (on average) an order of magnitude lower than that of the PM even in regional background sites. Bulk magnetic properties have been normalized by the mass of the material on the filters, but have been also considered as an absolute signal (e.g., magnetic moment) to provide an indication of the total load of magnetic particles. The total magnetic moment of each sample has been

calculated by assuming that the measured sister filters are representative for the magnetic properties of all the filters obtained for each sample.

We have used mass-specific magnetic susceptibility ($\chi$) as an initial indicator of the concentration of magnetic minerals on the filters (Liu et al., 2012). In order to assess the relative contribution of low- (magnetite, maghemite) versus high-coercivity (hematite, goethite) minerals to the remanence, we have computed the forward S-ratio (IRM@0.3T/IRM@1.2T) of Kruiver and Passier (2001). IRM@0.3T and the "hard" IRM (HIRM = IRM@1.2T-IRM@0.3T) have been used as proxies for the concentration of low- and high-coercivity minerals, respectively (Liu et al., 2012). Finally, the ratio IRM@1.2T/$\chi$ has been used as an indicator of the grain size of the magnetic minerals in the filters (Peters and Dekkers, 2003; Liu et al., 2012).

### 2.5. Geochemical data

One sister filter for each sample was used to quantify the concentration of major and trace elements. We followed the method of Querol et al. (2001), which involves complete digestion of the filters in a HF:$HNO_3$:$HClO_4$ solution, then drying and re-dissolution of the resulting mixture in $HNO_3$ (5% concentration), and its analysis by Inductively Coupled Plasma Atomic Emission Spectroscopy (ICP-AES) and Inductively Coupled Plasma Mass Spectrometry (ICP-MS). Blank filters were analysed along with each set of samples in order to account for filter contribution. We have used the concentrations of Al, Ti, Cu and Sb for comparison with environmental magnetic properties in order to establish their link with two of the most relevant natural and anthropogenic sources of atmospheric deposition expected in the studied sites, namely NAD (Al and Ti, Revuelta et al., 2014) and vehicular traffic (Cu and Sb, Amato et al., 2009; Revuelta et al., 2014). Geochemical measurements were performed at the Geochemistry Laboratory of IGME at Madrid using a VARIAN VISTA-MPX ICP-EAS and an AGILIENT 7500 CE ICP-MS.

## 3. Results

### 3.1. Rock magnetic characterization

Unmixing of IRM acquisition curves requires fitting the data with up to four distinctive components whose characteristics are consistent across the studied samples (Fig. 2, Table 2). Urban, industrial and agricultural samples are characterized by three components (Figs. 2a-d). Component 1 (C1) has a coercivity ($B_h$) of less than 10 mT ($\log_{10}$ B<1 in Fig. 2) and represents an average extrapolated contribution (EC) of 6% to the total IRM (Table 2). Component 2 (C2) has a coercivity ranging between 19 and 54 mT ($\log_{10}$ B =

1.2-1.8) and constitutes the bulk of the IRM, with an average contribution that is slightly larger in urban and industrial samples (78-96%) compared to the remaining settings (70-92%) (Table 2). Component 3 (C3) has an average coercivity of 760 mT ($\log_{10}$ B>2.7), and represent a fraction of the IRM ranging between 1 and 9 % (Table 2). The only exception to this pattern is one industrial sample, where C1 was not identified (MON-4.1, Table 2). In all but one sample associated with prominent NAD events, a fourth component (C4) with an average coercivity of ~125 mT ($\log_{10}$ B = 2-2.2) is required to provide an adequate fit to the data regardless of the site type (Fig. 2e-h). In these cases, the relative contribution of C3 increases slightly (5-9%) at the expense of C2, which shows a consistent shift to slightly lower coercivities ranging between 19 and 42 mT (Fig. 2) (Table 2). The four identified components exhibit dispersion parameters (DP) ranging typically from 0.25 to 0.4, although some values smaller and larger than 0.2 and 0.4, respectively, are also observed. S values range from 0.83 to 1.3 for the four components. We attribute the somewhat large DP and S values to the very small amount of material present in the filters, which often results in noisy IRM acquisition curves (see grey dots in Fig. 2) that needed to be smoothed before unmixing. These values call for a cautious interpretation of results, with the possibility of a mixed mineralogy within a single component being the most likely flaw (Heslop et al., 2004). Based on their coercivities, C1 and C2 can be associated with either magnetite or maghemite. C3 corresponds to hematite and might include a small fraction of goethite that is magnetized by the 1.2 T field. C4 has a coercivity that may correspond either to magnetite/maghemite or to hematite.

Hysteresis curves for all the studied samples are characterized, after correction of the high-field paramagnetic slope, by narrow loops that saturate between 300-500 mT (Fig. 3a-e). $B_{cr}$ values range between 17 and 33 mT and are somewhat higher in urban and industrial sites compared to agricultural, background, or urban samples with a prominent NAD load (Table 2). These values are similar to those reported in many studies of anthropogenic PM (e.g., Sagnotti et al., 2006, 2009; Saragnese et al., 2011), and indicate that low-coercivity minerals such as magnetite or maghemite dominate the magnetic properties of the samples. A minor contribution of high-coercivity minerals (e.g. hematite) to hysteresis properties could be inferred from the somewhat wasp-waisted shape of some hysteresis loops (Roberts et al., 1995), especially those of samples with a significant NAD load (Fig. 3b, d). Representation of hysteresis data on the Day plot (Day et al., 1977) indicates that urban samples fall just above the MD field, suggesting the dominance of coarse magnetite/maghemite particles (Fig. 3f). Urban samples with a

prominent NAD contribution move towards lower $B_{cr}/B_c$ values along the SD-MD mixing curve of Dunlop (2002), thereby indicating a relatively major contribution of finer SD or PSD (vortex) magnetic grains. Samples from industrial, agricultural and background sites with a prominent NAD load fall within the PSD domain, also indicating the relative importance of SD or vortex magnetic grains. Noticeably, all the studied samples fall slightly above the SD-MD mixing line of Dunlop (2002) regardless of sample type, which indicates the widespread contribution of ultrafine SP particles. Overall, hysteresis data confirm the complex mineralogical assemblage of the studied samples demonstrated by the IRM acquisition curves.

FORC distributions in urban site samples (Fig. 4a) are characterized by slightly asymmetric contour lines that diverge at a certain angle along the $B_i$ axis and include a low coercivity (<25 mT) tail along the $B_c$ axis. This feature is intermediate between those shown by MD particles, whose contour lines show an important divergence along the $B_i$ axis, and by vortex particles, whose contour lines tend to intersect the $B_i$ axis at right angles (Zhao et al., 2017). The associated remFORC distributions have a positive peak along the $B_c$ axis and a second, significantly smaller peak along the $B_i$ <0 mT axis. iFORC distributions are characterised by two positive and negative peaks along the $B_i > 0$ and $B_i < 0$ axis, respectively, plus some weaker, additional positive and negative peaks in the remainder of the diagram. Finally, the tFORC distributions are characterized by two positive peaks close to the $B_i > 0$ and $B_i < 0$ axis forming a butterfly-shaped pattern. The iFORC and tFORC features indicate the presence of both vortex and MD particles, although the relative width of the butterfly-shaped pattern suggests a greater contribution from vortex particles (Zhao et al., 2017). The small peak along the $B_i$ <0 mT axis in the remFORC points to thermal activation effects related with the presence of SP particles in urban samples. FORC distributions for samples from the MON industrial site are comparable to those found in urban sites, although the more divergent distribution along the $B_i$ axis in the FORC diagram and the narrower butterfly-shaped pattern in the tFORC distribution points to a greater fraction of MD particles. In contrast to urban and industrial site samples, samples from background locations with significant NAD loads appear to be dominated by a SD fraction that produces closed contour lines around a peak at <20 mT in the FORC distribution (Fig. 4b). Such SD particles are also inferred from the iFORC diagram, where a characteristic negative-positive-negative triple peak near the $B_i$-$B_c$ intersection can be identified despite of the surrounding noisy signal. The tFORC distribution is characterized by a butterfly-shaped pattern, which, along with the

asymmetric divergent distribution along the $B_i$ axis observed in the FORC diagram, indicates vortex particles (Zhao et al., 2017).

### 3.2. SEM observations

SEM images and EDS analyses demonstrate the frequent occurrence of iron oxides with different morphologies and grain sizes (Fig. 5). The most common form of iron oxide in urban and industrial samples is constituted by irregular aggregates that range between 2 and 40 μm in length and are formed by individual particles with irregular or spherical shapes and sizes varying between 0.2 and 2 μm (Fig. 5a-c). They also appear as isolated particles (Fig. 5d) or spherules that range between 0.5 and 10 μm and sometimes show the characteristic dendritic surface attributed to magnetite spherules formed by rapid quenching (Isobe and Gondo, 2013) (Fig. 5e). At MON industrial site, we observed some spherical aggregates with evidence for cracking (Fig. 5b). Aggregates and spherules often contain minor amounts of Zn, Mn or Cu, which, along with the observed textures, point to magnetite particles of anthropogenic origin (Petrovský and Ellwood, 1999; Sagnotti et al., 2006, Saragnese et al., 2011). Minor amounts of such anthropogenic irregular aggregates and spherules have also been found in background and agricultural sites as well. Background and urban samples encompassing distinctive NAD outbreaks are characterized by iron oxides with different morphologies and grain sizes of about 0.5 to 8 μm. Some iron oxides show the platy, hexagonal habit diagnostic of hematite crystals, which sometimes appear attached to the surface of large phyllosilicate aggregates (Fig. 5f). Other iron and iron-titanium oxide particles display elongated or equidimensional shapes with irregular, but smooth, surfaces (Fig. 5c). These features (Rodríguez-Navarro et al., 2018) point, along with the connection between these samples and distinctive NAD events, to an aeolian origin for these particles, that are also present in samples not related with important NAD events.

### 3.3. Bulk environmental magnetic properties

S-ratios from urban and industrial samples range typically between 0.94 and 1, in clear contrast with the lower (0.86-0.96) values found for background and agricultural sites (Fig. 6a) (Supplementary Table 1). Site median S-ratios between 0.96 and 0.98 in industrial and urban environments are significantly higher, based on their inter-quartile (IQ) ranges, than those of background and agricultural settings. These data indicate that a low-coercivity, magnetite-like mineral is dominating the magnetic properties of

atmospheric deposition at all sites, with a smaller contribution by hematite in urban and industrial sites that is relatively increased in background and agricultural areas.

The mass specific magnetic susceptibility ($\chi$) of urban samples ranges mostly between 3 and 8 x $10^{-6}$ $m^3$/kg, which is in contrast to those found in background sites (typically <2 x $10^{-6}$ $m^3$/kg and often exhibiting negative values) (Fig. 6b). This points to higher concentrations of magnetic minerals in urban areas compared to background contexts, where $\chi$ is often dominated by diamagnetic contributions. Remanence values support these inferences, higher IRM@0.3T values, and hence magnetite abundances, are found in urban sites compared with those in background areas (Fig. 6c). The exception to this pattern is Ebro valley, where S-ratios, $\chi$, and IRM@0.3T values of the urban (ZGZ) and industrial (MON) sites are somewhat smaller than in other cities, while also being comparatively higher in background (and agricultural) sites. This results in the overlap of IQ ranges between urban/industrial and background/agricultural sites. HIRM tends to be higher in urban/industrial than in background/agricultural sites although the differences are small (Fig. 6d), indicating that the concentration of hematite, as opposed to magnetite, is comparable across the set of studied environments.

IRM@1.2T/$\chi$ values of urban samples cluster around site median values that range between 4.6 and 7.7 kA/m (Fig. 6e). This contrasts with IRM@1.2T/$\chi$ of background and agricultural sites, which varies between -19 and >29 kA/m. The combination of negative and exceedingly large values is an artefact caused by the either negative or near-zero susceptibilities in these samples, which results in unreliable IRM@1.2T/$\chi$ estimates with no physical meaning. In contrast, the narrow range of IRM@1.2T/$\chi$ found in urban samples, were $\chi$ is dominated by large concentrations of magnetite, point to a narrow grain size either spanning the SP/SD boundary (<30 nm) or the coarse MD state (10-20 μm) (see Peters and Dekkers, 2003). Combined hysteresis, FORC and SEM data suggest that the latter situation is much more likely. Slightly larger IRM@1.2T/$\chi$ values in industrial samples (median of 12 kA/m) point to finer MD magnetite grains between 2 and 10 μm (Peters and Dekkers 2003).

Time variations in mass-specific magnetic parameters in cities and their closest background sites reveal significant features (Fig. 7). Thus, $\chi$ shows little variation throughout the studied period at all urban sites with the exception of the winter season, when $\chi$ increases significantly. Significant $\chi$ peaks are also observed during fall and spring in BCN and PMI. As expected, $\chi$ variations are broadly mimicked by changes in IRM@0.3T. The situation is different in background sites, where the only remarkable

features in χ are the decreases observed during winter at all sites except HJM. Minor IRM@0.3T variations are observed throughout the year at all background sites with the exception of CHI, where a significant increase is observed during the winter. No distinctive HIRM variations are observed at any of the sites throughout the year. It is noticeable that most variations observed in χ and IRM@0.3T are contained within the protracted period of winter anticyclonic conditions experienced by the Iberian Peninsula between December 2016 and January 2016, which led to stagnant conditions and dry accumulations of very low amounts of PM. It is also noticeable that prominent NAD outbreaks, signalled by clear peaks in the amount of PM, did not alter significantly the χ, IRM@0.3T and HIRM values.

### 3.4. Geochemical data

Cu loads, expressed as fluxes to account for differences in sampling time and collector area, span an order of magnitude regardless of site type (Fig. 8). The correlation between Cu and IRM@0.3T, also expressed as a flux, is moderate, poor or even non-existent in most cases, although at some sites it appears to be meaningful (Fig. 8D) (Table 3). The correlation of IRM@0.3T with Sb, another proxy for vehicular PM (Revuelta et al., 2014, more), is somewhat weaker, even for urban sites (Table 3). The correlation between Al and HIRM is significantly stronger in most cases, regardless the type of site, a situation that is also found for the correlation between HIRM and Ti, another proxy for NAD loads (Revuelta et al., 2014). These correlations are better elucidated when Cu, IRM@0.3T, Al and HIRM fluxes are plotted as a function of time for all the studied sites (Figs. 9 and 10). The high correlation coefficients (R) observed between Al and HIRM are reflected in the close similarity observed in the variations of both parameters (Fig. 9). Thus, they do not only consistently delineate the most distinctive NAD events, but also smaller variations throughout the rest of the monitored period (Fig. 9). Cu and IRM@0.3T do not covary at most sites as clearly as Al and HIRM do (Fig. 10), and also appear to be affected by some of the most distinctive NAD events.

## 4. Discussion

### 4.1. Origin of magnetic minerals in atmospheric deposition

IRM component C1 is similar to a low coercivity (~10 mT) component associated by Sagnotti et al. (2006) to large MD magnetite/maghemite grains that result from the abrasion of metallic parts of cars, especially brakes and tyres in Rome. Hysteresis (Fig. 3), FORC (Fig. 4a,b) and SEM (Fig. 5d) data demonstrate the presence of large MD grains

in urban and industrial sites and, hence, validate the association of C1 with MD magnetite/maghemite grains derived mainly from vehicular traffic in urban and industrial areas. C1 is also present in agricultural and background sites (Fig. 2); while C1 in the former might be related to agricultural vehicles, its presence in background sites suggests that at least part of the emissions produced by traffic in urban and industrial environments reaches these sites via atmosphere mixing.

Regarding IRM component C2, which is characterized by coercivities between 19 and 54 mT and is therefore linked to magnetite/maghemite, our data indicate that it constitutes the bulk of the magnetization in all studied samples (Fig. 2). The observation that IRM@0.3T values are distinctly higher in urban and industrial sites compared to agricultural and background areas (Fig. 6) suggests that this dominant magnetite/maghemite component is related to anthropogenic activity. This interpretation is further supported by hysteresis (Fig. 3), FORC (Fig. 4a,b) and SEM (Fig. 5a-e) data, which collectively show that vortex and MD magnetite/maghemite grains of anthropogenic origin dominate the magnetic assemblage of the studied samples. Given that vehicular exhausts are the main source of pollution in urban areas (Muxworthy et al., 2003; Sagnotti et al., 2006, 2009; Saragnese et al., 2011; Revuelta et al., 2014), and that C1 is related to abrasion of vehicular brakes and tyres, the most likely interpretation is that C2 is linked to vehicular exhaust emissions. It should be noted, however, that IRM components with average coercivities similar to those of C2 have been attributed to pedogenic (Maxbauer et al., 2016) or aeolian (Sagnotti et al., 2006; Font et al., 2018) magnetite particles, which raises the question of whether this component results from a combination of anthropogenic and natural sources as has been previously documented in other European cities (Spassov et al., 2004). Three lines of evidence support the hypothesis that C2 includes a mixture of natural and anthropogenic particles: 1) C2 has somewhat lower coercivities (19 to 42 mT) in samples with significant NAD loads, regardless of their type (Fig. 2, Table 1), when compared with standard urban and industrial samples (36-54 mT); 2) aeolian magnetite particles are often reported at urban sites in association with irregular magnetite/maghemite aggregates of anthropogenic origin (Fig. 5c); and 3) the somewhat large DP values associated to C2 are prone to result from the combination of more than one magnetic assemblage in a single component (Heslop et al., 2004). We interpret that in urban and industrial sites, aeolian magnetite is masked by a larger fraction of anthropogenic magnetite particles. The slightly higher coercivity of the latter would be linked to the presence of coarse MD magnetite grains rimmed by a layer of interacting, SP maghemite particles (Muxworthy et al., 2003;

Sagnotti et al., 2009; Saragnese et al., 2011; Revuelta et al., 2014). As with C1, the presence of a pervasive C2 in background sites suggest that emissions produced by traffic in urban and industrial environments reaches these sites via atmospheric mixing. When NAD loads are important, it is the larger, softer aeolian magnetite that masks the anthropogenic magnetite/maghemite even in urban sites, resulting in an overall shift to lower coercivities. Hysteresis (Fig. 3) and FORC (Fig. 4) data indicate that this aeolian magnetite occurs mainly as SD or vortex particles, in agreement with results from Revuelta et al. (2014).

IRM component C3 has a high coercivity (average of 740 mT) that is typically linked with aeolian hematite (Maxbauer et al., 2016; Font et al., 2018) and a grain size mostly spanning the SD range (Roberts et al., 2020). The presence of this component at all sites, including urban areas where production of local dust appears unlikely due to the dearth of bare soil, suggests a Saharan origin for this aeolian component, which is supported by its larger relative importance in samples with significant NAD loads (Fig. 2, Table 1). The main Saharan origin for this hematite component is apparent in the Ebro Basin, where the background magnetic signal appears to be enriched in high-coercivity minerals, as indicated by the excellent correlation observed in this area between HIRM and proxies for NAD abundances (Al and Ti) (Fig. 9b, Table 3).

With regard to IRM component C4, its exclusive association with significant NAD loads demonstrates a clear aeolian origin. Its coercivity (~125 mT) appears to be too hard for non-biogenic magnetite, but would be consistent with hematite grains larger (MD) than higher-coercivity hematite associated to C3 (Roberts et al., 2020). In this regard, it is important to note that C3 (mainly SD hematite) appears to be linked to background NAD fluxes identified in all the samples, whereas C4 (likely MD hematite) appears to be linked to only the major NAD outbreaks. This points to the arrival of hematite from a different Saharan source during these major periods. We tentatively link the background hematite of C3 to the coastal areas of the western Sahara (dust source area 2 of Scheuvens et al., 2013) and the additional hematite of C4 to the interior areas of southern Algeria and northern Mali (dust source area 3 of Scheuvens et al., 2013), where warmer and drier conditions favour enhanced hematite formation (Larrasoaña et al., 2015) in surface silts that constitute the main dust source (Prospero et al., 2002).

### 4.2. Environmental significance of bulk magnetic properties

In order to use bulk magnetic parameters as proxies for natural or antropogenic processes, their environmental significance needs to be determined. Of particular

591 importance to this study are IRM@0.3T and HIRM, which are candidate proxies for
592 monitoring pollution and NAD fluxes via concentrations of anthopogenic
593 magnetite/maghemite and natural (aeolian) hematite, respectively. The correlation
594 between IRM@0.3T and proxies for anthropogenic pollution (Cu or Sb) is not good for
595 all sites (Fig. 8, Table 3), and this might be explained by different factors. First, Cu and
596 Sb loads are preferably incorporated into the soluble fraction of atmospheric deposition,
597 whereas anthropogenic magnetite/maghemite concentrations correspond to PM
598 accumulated on the filters. Second, Cu and Sb are mainly linked to vehicular traffic
599 (Amato et al., 2009; Revuelta et al., 2014), whereas anthropogenic magnetite/maghemite
600 particles reported here may also be sourced from industrial activities around urban areas.
601 Third, C2 appears to be a mixture of natural magnetite and anthropogenic
602 magnetite/maghemite particles, whose separation by means of the measured bulk
603 magnetic properties is not possible. These circumstances indicate, in a context where
604 NAD supply occurs throughout the year (Pey et al., 2013, Varga et al., 2014), that
605 inferences concerning anthropogenic pollution based on IRM@0.3T or other proxies for
606 magnetite abundance should be treated with caution.
607 With regards to hematite, no evidence for its occurrence as an anthropogenic mineral
608 has been found in our study, in line with most environmental magnetic studies of PM
609 (Petrovský and Ellwood, 1999; Muxworthy et al., 2002, 2003; Spassov et al., 2004;
610 Sagnotti et al., 2006, 2009; Saragnese et al., 2011; Revuelta et al., 2014; Hofman et al.,
611 2017; Tan et al., 2018). Therefore, the reliability of HIRM as a proxy for NAD flux relies
612 on the choice of the magnetic fields used to impart the laboratory remanences from which
613 HIRM is estimated. Thus, using IRM@1.2T and IRM@0.3T to calculate HIRM means
614 that remanence carried by hematite with a coercivity <300 mT will be lost and result in
615 underestimation of hematite content (Roberts et al., 2020). This will have occurred with
616 the low-coercivity tail of C3 and the majority of C4 (see Fig. 2). Yet, the choice of a 0.3
617 T field to estimate HIRM ensures that the contribution of the high-coercivity tail of C2 to
618 HIRM, most likely associated with anthropogenic magnetite by virtue of its higher
619 coercivity, is minimal so that the correlation of HIRM with NAD proxies is still apparent
620 (Fig. 8, Table 3). Our results demonstrate that although HIRM based on IRM@0.3T
621 misses part of the genuine NAD hematite contribution, it avoids contamination by a
622 spurious, anthropogenic signal and, thus, can be used as a proxy for NAD flux.
623
624 4.3. Temporal variations in NAD and pollution

HIRM and Al contents indicate that the flux of NAD is somewhat higher during summer at most network sites compared with winter (Fig. 9a-c). Superimposed on this overall trend of background NAD are major dust outbreaks identified at different monitoring stations, mainly at the beginning and end of winter but also during summer. These events are delineated by sharp peaks in both hematite and elemental (Al and Ti) fluxes that span typically one (e.g. ORD, ADV) or two (FRI, BCN) samples (Fig. 9). Exceptions to this are background sites ENO and ORG, in the westernmost part of the Cantabrian-Pyrenean region, and industrial and urban sites MON and PMI, respectively. Very low NAD fluxes occurred at ENO and, to lesser extent, ORG, where only the two major NAD outbreaks identified in late fall and late winter are detected. At MON and PMI, most of the winter season is characterised by sustained high fluxes of hematite that are somehow decoupled from Al fluxes. A possible explanation for such decoupling would be an additional, anthropogenic source of hematite linked to industrial pollution in MON, and potentially leisure cruise activity in PMI (Cerro et al., 2020). Overall, HIRM values corroborate the larger NAD background reported in previous studies for the Iberian Peninsula during the summer, and also the preferential transport of NAD over the eastern half of the peninsula and the Mediterranean basin (Querol et al., 2009; Varga et al., 2014; Pey et al., 2013, 2020).

In contrast to HIRM, IRM@0.3T values show no significant variations throughout the year. At ORD, ZGZ and EDC, a slight increase in IRM@0.3T may occur during summer (Fig. 10). Such an increase appears to occur in parallel with an increase in hematite flux, raising the question of whether such a subtle rise in magnetite fluxes is linked, at least partially, to supply of background NAD rather than anthropogenic (pollution) fluxes. This may be the case because most of the major NAD outbreaks occurred during late autumn and late winter, which in many cases are associated with a noticeable increase in aeolian magnetite flux. Yet, the large Cu peaks associated with some (but not all) of these outbreaks suggest that part of the rise in magnetite abundances is linked to pollution, which might be explained by the compression of the mixing layer during NAD outbreaks and the resulting magnification of pollution (Pandolfi et al., 2014; Cerro et al., 2020). An alternative explanation to this parallel increase in magnetite and Cu might be entrainment of pollution by dust-laden desert winds as they pass over urban and industrial areas of NW Africa on their way to the Iberian Peninsula (Rodríguez et al., 2011). Regardless, the clearest indication that background IRM@0.3T values are ultimately linked to a dominant, anthropogenic source is that urban (PAM, ZGZ, BCN, PMI) and industrial (MON) sites have overall higher IRM@0.3T values when compared with their nearest

660 background locations (ORG, CHI, MSY, HJM). The rather constant IRM@0.3T values
661 observed throughout the year at most sites point to a steady supply of pollution or,
662 alternatively, indicate that magnetite/maghemite fluxes vary at timescales shorter (e.g.
663 working days versus weekends) than our biweekly sampling period.
664
665 **5. Conclusions**
666 Our study has enabled identification of three main magnetic mineral components in
667 the particulate fraction of atmospheric deposition collected at different environments in
668 Spain. Components C1 and C2 have low coercivities and are associated mainly with
669 coarse (PSD/vortex and MD) magnetite grains, likely coated with SP maghemite. These
670 anthropogenic particles are derived mostly from vehicular traffic and, possibly also,
671 industrial activities, which is consistent with findings for most European cities
672 (Muxworthy et al., 2002, 2003; Spassov et al., 2004; Sagnotti et al., 2006, 2009;
673 Saragnese et al., 2011; Sagnotti and Winkler, 2012; Revuelta et al., 2014, Hofman et al.,
674 2017). Our results indicate that anthropogenic magnetite/maghemite particles are
675 ubiquitous in pristine environments because of atmospheric transport. The third
676 component, C3, is related to SD hematite of aeolian origin and appears to represent a
677 baseline of NAD transported from the Sahara throughout most of the year. Such a natural
678 hematite fraction has been identified in other large cities within the Mediterranean region
679 of Europe (e.g. Rome, Sagnotti et al., 2006), and is likely to correspond to the subdued
680 (and often overlooked) high-coercivity component reported in other southern European
681 cities (Saragnese et al., 2011; Revuelta et al., 2014). When samples include distinctively
682 intense events of NAD deposition, a fourth component associated with coarser aeolian
683 hematite particles, possibly sourced from different areas within the Sahara, is also
684 identified regardless the site type.
685 Our results demonstrate that part of the magnetite/maghemite associated to C2 appears
686 to be of aeolian origin, a circumstance that has been reported in previous studies (Spassov
687 et al., 2004; Sagnotti et al., 2006; Revuelta et al., 2014). This seems to explain, along with
688 other factors, the somewhat moderate correlation observed between
689 magnetite/maghemite abundances and proxies for vehicular traffic, and demonstrates the
690 need for caution when interpreting environmental magnetic proxies for
691 magnetite/maghemite abundances in terms of anthropogenic loads. This would be
692 especially the case in southern European cities, where a steady supply of NAD occurs
693 throughout most of the year, and possibly also in other regions (middle East, SE Asia,
694 Australia, SW USA) located near deserts (see Prospero et al., 2002). In contrast, our

results show a reasonable correlation between hematite abundance and geochemical proxies for NAD supply (Al and Ti), and therefore indicate that environmental magnetic proxies of hematite abundances (HIRM) can be used to monitor the contribution of natural sources to atmospheric deposition.

**Acknowledgements**

We are grateful to P. Zuazo and J. Vera (Regional Government of Navarra), G. Sánchez and P. Pérez Colomina (Regional Government of Aragón), P. Elías (Regional Government of the Balearic Islands), N. Fernández (Zaragoza City Council), A. Herrero and A.M. López (Frigiliana City Council), A. Mora (Picos de Europa National Park), E. Villagrasa (Ordesa and Monte Perdido National Park), J. Gómez and E. Gerendiain (Garrapo S.L.), and C. Salas (VIESGO S.L.) for their administrative support and permision to access the facilities used in this project. A special thank is also given to A. Tejedor (Picos de Europa National Park), F. Bayo (Aguirre S.L.) and the personnel of the Ordesa y Monte Perdido National Park for their technical support during development of the project. This study was funded by the Spanish Agencia Estatal de Investigación and the European Funds for Regional Development (AEI/FEDER, UE) via the DONAIRE (CGL2015-68993-R) project. XZ and DH were supported by Australian Council Discovery Project DP200100765.

**Author contributions**

J.C. Larrasoaña and J. Pey designed the study and performed the data analysis. Sampling and mainteinance of the DONAIRE network was performed by J.C. Larrasoaña (Navarra), J. Pey and T. Mochales (Aragón), N. Pérez (Cataluña), J.C. Cerro and M.L. Tobar (Balearic Islands), M.P. Mata (Picos de Europa), and S. Castillo (Frigiliana). IRM acquisition curves, hystereis and FORC measurements were performed by X. Zhao and D. Heslop, whereas bulk magnetic measurements were conducted by J.C. Larrasoaña, E. Beamud and T.Mochales. J. Reyes and M.P. Mata were responsible for the obtention and interpretation of geochemical and SEM data, respectively. J.C. Larrasoaña wrote the article with inputs from all the co-authors in different sections of the article.

**References**

Abbasi, S., Keshavarzi, B., Moore, F., Hopke, P. K., Kelly, F. J., Dominguez, A. O., 2020. Elemental and magnetic analyses, source identification, and oxidative potential of

729 airborne, passive, and street dust particles in Asaluyeh County, Iran. Science of the
730 Total Environment 707, 136132.
731 Amato, F., Pandolfi, M., Escrig, A., Querol, X., Alastuey, A., Pey, J., Pérez, N., Hopke,
732 P., 2009. Quantifying road dust resuspension in urban environment by multilinear
733 engine: a comparison with PMF2. Atmospheric environment 43, 2770–2780.
734 Cao, L., Appel, E., Hu, S., Yin, G., Lin, H., Rösler, W., 2015. Magnetic response to air
735 pollution by soil and dust-loaded leaves in a changing industrial environment.
736 Atmospheric Environment 119, 304–313.
737 Cerro, J. C., Cerdà, V., Caballero, S., Bujosa, C., Alastuey, A., Querol, X., Pey, J., 2020.
738 Chemistry of dry and wet atmospheric deposition over the Balearic Islands, NW
739 Mediterranean: source apportionment and African dust areas. Science of the Total
740 Environment 747, 141187.
741 Day, R., Fuller, M. D., Schmidt, V. A., 1977. Hysteresis properties of titanomagnetites:
742 grain size and composition dependence. Physics of the Earth and Planetary Interiors
743 13, 260–266.
744 Dunlop, D. J., 2002. Theory and application of the Day plot (Mrs/Ms versus Hcr/Hc): 1.
745 Theoretical curves and tests using titanomagnetite data. Journal of Geophysical
746 Research 107, 2056.
747 Evans, M. E., and Heller, F. (2003). *Environmental Magnetism: Principles and*
748 *Applications of Enviromagnetics*. San Diego: Academic Press.
749 Font, E., Adatte, T., Andrade, M., Keller, G., Bitchong, A., M., Carvallo, C., Ferreira, J.,
750 Diogo, Z., Mirão, J., 2018. Deccan volcanism induced high-stress environment during
751 the Cretaceous–Paleogene transition at Zumaia, Spain: Evidence from magnetic,
752 mineralogical and biostratigraphic records. Earth and Planetary Science Letters 484,
753 53–66.
754 Heslop, D., McIntosh, G., Dekkers, M. J., 2004. Using time- and temperature-dependent
755 Preisach models to investigate the limitations of modelling isothermal remanant
756 magnetization acquisition curves with cumulative log Gaussian functions.
757 Geophysical Journal International 157, 55–63.
758 Hofman, J., Maher, B. A., Muxworthy, A., Wuyts, K., Castanheiro, A., and Samson, R.
759 (2017). Biomagnetic monitoring of atmospheric pollution: a review of magnetic
760 signatures from biological sensors. Environmental Science and Technology 51, 6648–
761 6664.

762 Isobe, H., Gondo, T., 2013. Dendritic magnetite crystals in rapid quenched fine spherules
763 produced by falling experiments through the high temperature furnace with controlled
764 gas flow. Journal of Mineralogical and Petrological Sciences 108, 227–237.
765 Kruiver, P. P., Passier, H. F., 2001. Coercivity analysis of magnetic phases in sapropel
766 S1 related to variations in redox conditions, including an investigation of the S ratio.
767 Geochemistry Geophysics Geosystems 2, GC000181.
768 Kruiver, P. P., Dekkers, M. J., Heslop, D., 2001. Quantification of magnetic coercivity
769 components by the analysis of acquisition curves of isothermal remanent
770 magnetisation. Earth and Planetary Science Letters 189, 269–276.
771 Larrasoaña, J. C., Roberts, A. P., Liu, Q. S., Lyons, R., Oldfield, F., Rohling, E. J.,
772 Heslop, D., 2015. Source-to-sink magnetic properties of NE Saharan dust in Eastern
773 Mediterranean marine sediments: review and paleoenvironmental implications.
774 Frontiers in Earth Science 3, 19.
775 Lehndorff, E., Urbat, M., Schwar, L., 2006. Accumulation histories of magnetic particles
776 on pine needles as function of air quality. Atmospheric Environment 40, 7082–7096.
777 Liu, Q. S., Roberts, A. P., Larrasoaña, J. C., Banerjee, S. K., Guyodo, Y., Tauxe, L., and
778 Oldfield, F. (2012a). Environmental magnetism: principles and applications. *Rev.*
779 *Geophys.* 50, RG4002, doi:10.1029/2012RG000393.
780 Maher, B. A., Ahmed, I. A. M., Karloukovski, V., MacLaren, D. A., Foulds, P. G., Alison,
781 D., Mann, D. M. A., Torres-Jardón, R., Calderon-Garciduenas, L., 2016. Magnetite
782 pollution nanoparticles in the human brain. Proceedings of the National Academy of
783 Sciences of the United States of America 113, 10797–10801.
784 Matzka, J., Maher, B. A., 1999. Magnetic biomonitoring of roadside tree leaves:
785 identification and spatial and temporal variations in vehicle derived particles.
786 Atmospheric Environment 33, 4565–4569.
787 Maxbauer, D. P., Feinberg, J. M., Fox, D. L., 2016. MAX UnMix: A web application for
788 unmixing magnetic coercivity distributions. Computers & Geosciences 95, 140–145.
789 Muxworthy, A. R., Schmidbauer, E., Petersen, N., 2002. Magnetic properties and
790 Mössbauer spectra of urban atmospheric particulate matter: a case study from Munich,
791 Germany. Geophysical Journal International 150, 558–570.
792 Muxworthy, A. R., Matzke, J., Davila, A. F., Petersen, N., 2003. Magnetic signature of
793 daily sampled urban atmospheric particles. Atmospheric Environment 37, 4163–4169.
794 Pandolfi, M., Tobias, A., Alastuey, A., Sunyer, J., Schwrtz, J., Lorente, J., Querol, X.,
795 2014. Effect of atmospheric mixing layer depth variations on urban air quality and

daily mortality during Saharan dust outbreaks. Science of the Total Environment 494–495, 283–289.

Petrovský, E., Ellwood, B.B., 1999. Magnetic monitoring of air- land- and water-pollution. In: Maher, B. A., Thompson, R. (Eds.), Quaternary Climates, Environments and Magnetism. Cambridge University Press, New York, pp. 279–322.

Peters, C., Dekkers, M. J., 2003. Selected room temperature magnetic parameters as a function of mineralogy, concentration and grain size. Physics and Chemistry of the Earth 28, 659–667.

Pey, J., Querol, X., Alastuey, A., Forastiere, F., Stafoggia, M., 2013. African dust outbreaks over the Mediterranean Basin during 2001-2011: $PM_{10}$ concentrations, phenomenology and trends, and its relationship with synoptic and mesoscale meteorology. Atmospheric Chemistry and Physics 13, 1395–1410.

Pey, J., Larrasoaña, J. C., Pérez, N., Cerro, J. C., Castillo, S., Tobar, M. L., de Vergara, A., Vázquez, I., Reyes, J., Mata, M. P., Mochales, T., Orellana, J. M., Causapé, J., (2020). Phenomenology and geographical gradients of atmospheric deposition in southwestern Europe: Results from a multi-site monitoring network. Science of the Total Environment 744, 140745.

Prospero, J. M., Ginoux, P., Torres, O., Nicholson, S. E., Gill, T. E., 2002. Environmental characterization of global sources of atmospheric soil dust identified with the Nimbus 7 total ozone mapping spectrometer (TOMS) absorbing aerosol product: Reviews of Geophysics 40, 1002.

Querol, X., Alastuey, A., Pey, J., Cusack, M., Pérez, N., Mihalopoulos, N., Theodosi, C., Gerasopoulos, E., Kubilay, N., Koçak, M., 2009. Variability in regional background aerosols within the Mediterranean. Atmospheric Chemistry and Physics 9, 4575–4591.

Revuelta, M. A., McIntosh, G., Pey, J., Pérez, N., Querol, X., Alastuey, A., 2014. Partitioning of magnetic particles in $PM_{10}$, $PM_{2.5}$ and $PM_1$ aerosols in the urban atmosphere of Barcelona (Spain). Environmental Pollution 188, 109–117.

Rodríguez, S., Alastuey, A., Alonso, Pérez, S., Querol, X., Cuevas, E., Abreu-Alonso, J., Viana, M., Pérez, N., Pandolfi, M., de la Rosa, J., 2011. Transport of desert dust mixed with North African industrial pollutants in the subtropical Saharan Air Layer. Atmospheric Chemistry and Physics 11, 6663–6685.

Rodríguez-Navarro, C., di Lorenzo, F., Elert, K., 2018. Mineralogy and physicochemical features of Saharan dust wet deposited in the Iberian Peninsula during extreme red rain events. Atmospheric Chemistry and Physics 18, 10089–10122.

Roberts, A. P., Cui, Y., Verosub, K. L., 1995. Wasp-waisted hysteresis loops: mineral magnetic characteristics and discrimination of components in mixed magnetic systems. Journal of Geophysical Research 100, 17909–17924.

Roberts, A. P., Tauxe, L., Heslop, D., Zhao, X., Jiang, Z., 2020. A critical appraisal of the "Day" diagram. Journal of Geophysical Research: Solid Earth 123, 2618–2644.

Roberts, A. P., Zhao, X., Heslop, D., Abrajevitch, Chen, Y. H., Hu, P., Jiang, Z., Liu, Q., Pillans, B. J., 2020. Hematite (α-Fe2O3) quantification in sedimentary magnetism: limitations of existing proxies and ways forward. Geoscience Letters 7, 8.

Sagnotti, L., Macrì, P., Egli, R., Mondolino, M., 2006. Magnetic properties of atmospheric particulate matter from automatic air sampler stations in Latium (Italy): toward a definition of magnetic fingerprints for natural and anthropogenic $PM_{10}$ sources. Journal of Geophysical Research 111, B12S22.

Sagnotti, L., Taddeucci, J., Winkler, A., Cavallo, A., 2009. Compositional, morphological, and hysteresis characterization of magnetic airborne particulate matter in Rome, Italy. Geochemistry Geophysics Geosystems 10, Q08Z06.

Sagnotti, L., Winkler, A., 2012. On the magnetic characterization and quantification of the superparamagnetic fraction of traffic-related urban airborne PM in Rome, Italy. Atmospheric Environment 59, 131–140.

Saragnese, F., Lanci, L., Lanza, R., 2011. Nanometric-sized atmospheric particulate studied by magnetic analyses. Atmospheric Environment 45, 450–459.

Scheuvens, D., Schütz, L., Kandler, K., Ebert, M., weinbruch, S., 2013. Bulk composition of norther African dust and its source sediments – A compilation. Earth-Science Reviews 116, 170–194.

Spassov, S., Egli, R., Heller, F., Nourgaliev, D. K., Hannam, J., 2004. Magnetic quantification of urban pollution sources in atmospheric particulate matter. Geophysical Journal International 159, 555–564.

Tan, Z., Lu, S., Zhao, H., Kai, X., Jiaxian, P., Win, M. S., Yu, S., Yonemochi, S., Wang, Q., 2018. Magnetic, geochemical characterization and health risk assessment of road dust in Xuanwei and Fuyuan, China. Environmental Geochemistry and Health 40, 1541–1555.

Varga, G., Újvári, Kovács, J., 2014. Spatiotemporal patterns of Saharan dust outbreaks in the Mediterranean Basin. Aeolian Research 15, 151–160.

WHO, 2006. Air quality guidelines for particulate matter, ozone, nitrogen dioxide and sulfur dioxide. In: Global Update 2005. Summary of Risk Assessment. World Health Organization.

865 Zhao, X., Heslop, D., Roberts, A. P., 2015. A protocol for variable resolution first-order
866 reversal curve measurements. Geochemistry Geophysics Geosystems 16, 1364–1377.
867 Zhao, X., Roberts, A. P., Heslop, D., Paterson, G. A., Li, Y., Li, J., 2017. Magnetic
868 domain state diagnosis using hysteresis reversal curves. Journal of Geophysical
869 Research: Solid Earth 122, 4767–4789.
870

**Figure captions**

**Figure 1.** Sampling procedures. (A) Location of the studied sites. (B) Example of a collector installed on an air quality station. (C) Plastic containers partially filled with water after sampling. (D) Detail of the filtering process. (E) Example set of filters.

**Figure 2.** Unmixing of selected IRM acquisition curves using MAX UnMix (Maxbauer et al., 2016). Grey dots and the yellow curve represent the smoothed IRM data and modelled coercivity distribution, respectively. Shaded areas represent 95% confidence intervals associated with each component. (A) to (D) show representative samples from urban, industrial and agricultural sites. (E) to (H) show representative samples from background, urban and agricultural sites with a significant contribution from North African Dust (NAD).

**Figure 3.** Hysteresis loops of representative samples collected in urban (A), industrial (B) and agricultural (C) sites. (D) and (E) correspond to urban and background samples with a significant contribution from North African Dust (NAD). (F) Day diagram of the studied samples according to their type.

**Figure 4.** Sequence of different types of FORC diagrams measured for representative urban (A) and background samples with a significant contribution from North African Dust (NAD) (B), measured following Zhao et al. (2017). SF denotes the smoothing factor, and NF stands for non-linear factor in the colour scale.

**Figure 5.** Back-scattered electron microscope images of selected samples. (A) Anthropogenic iron oxide aggregate in urban sample BCN-6. (B) Anthropogenic, spherical iron oxide aggregate in industrial sample MON-10. (C) Mixture of anthropogenic iron-oxide aggregates (white arrows) and aeolian Fe-Ti oxide particles (dashed white arrows) in an urban sample with significant NAD load (PAM-12). (D) Large, anthropogenic iron-oxide particle (white arrow) in urban sample BCN-6. (E) Anthropogenic magnetite dendritic spherule from the sample shown in C9 (PAM-12). (F) Platy iron-oxides, often showing an hexagonal habit, attached to a large aeolian particle (white arrow) in a background sample with significant NAD load (ORD-13).

**Figure 6.** Bulk environmental magnetic parameters for the studied sites. (A) S-ratio. (B) Mass-specific magnetic susceptibility. (C) Mass-specific IRM@0.3T. (D) Mass-specific

HIRM. (E) IRM@1.2T/$\chi$. Red, black, orange and green symbols denote urban, industrial, agricultural and regional background sites, respectively.

**Figure 7.** Temporal variations in mass-specific environmental magnetic parameters for the studied urban sites, which are shown along with their nearest regional background site. Orange arrows indicate samples affected by significant NAD loads (Pey et al., 2020).

**Figure 8.** Scatter plots of IRM@0.3T versus Cu fluxes, and of HIRM versus Ti fluxes, for samples representative for urban (A), agricultural (B), industrial (C) and background (D) sites.

**Figure 9.** Temporal variations in the fluxes of HIRM and Ti for the studied sites in(A) the Cantabrian-Pyrenean region, (B) the Ebro Valley, and (C) the Mediterranean region. Orange arrows mark significant NAD breakouts as identified by Pey et al. (2020).

**Figure 10.** Temporal variations in IRM@0.3T and concentration of Cu for the studied sites. Both magnetizations and elemental concentrations are normalized by surface and day. Orange arrows mark significant NAD breakouts as identified by Pey et al. (2020).

**Table 1.** Characteristics of the studied sites, which include the abbreviations used throughout the paper, the type, geographical latitude and longitude, altitude, annual rainfall (Pey et al., 2020), and start and end of the monitoring period for each site. Asterisks mark the natural sites that act as the regional background for the urban and industrial sites listed immediately above.

**Table 2.** Hysteresis and IRM unmixing data for the studied samples. *Bh*, *DP*, *S* and *EC* stand for the mean coercivity, dispersion parameter, skewness and extrapolated contribution associated to each component.

**Table 3.** Correlation coefficient (R) between IRM@0.3T and Cu, IRM@0.3T and Sb, HIRM and Al, and HIRM and Ti fluxes for the studied sites. Bold numbers denote R values larger than 0.7, considered to represent a strong correlation.

Figure 1

Click here to access/download;Figure;Figure-1.pdf

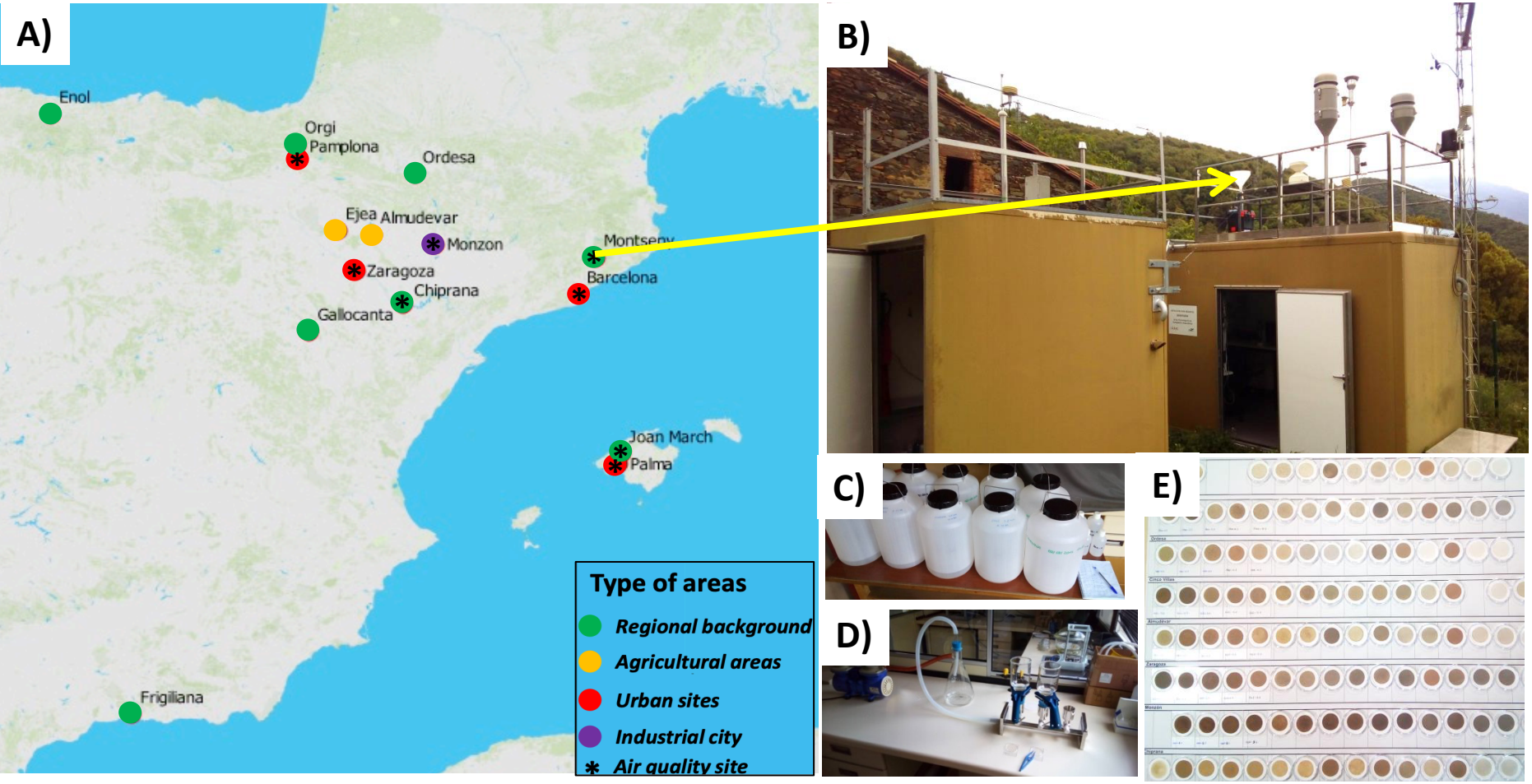

Figure 2



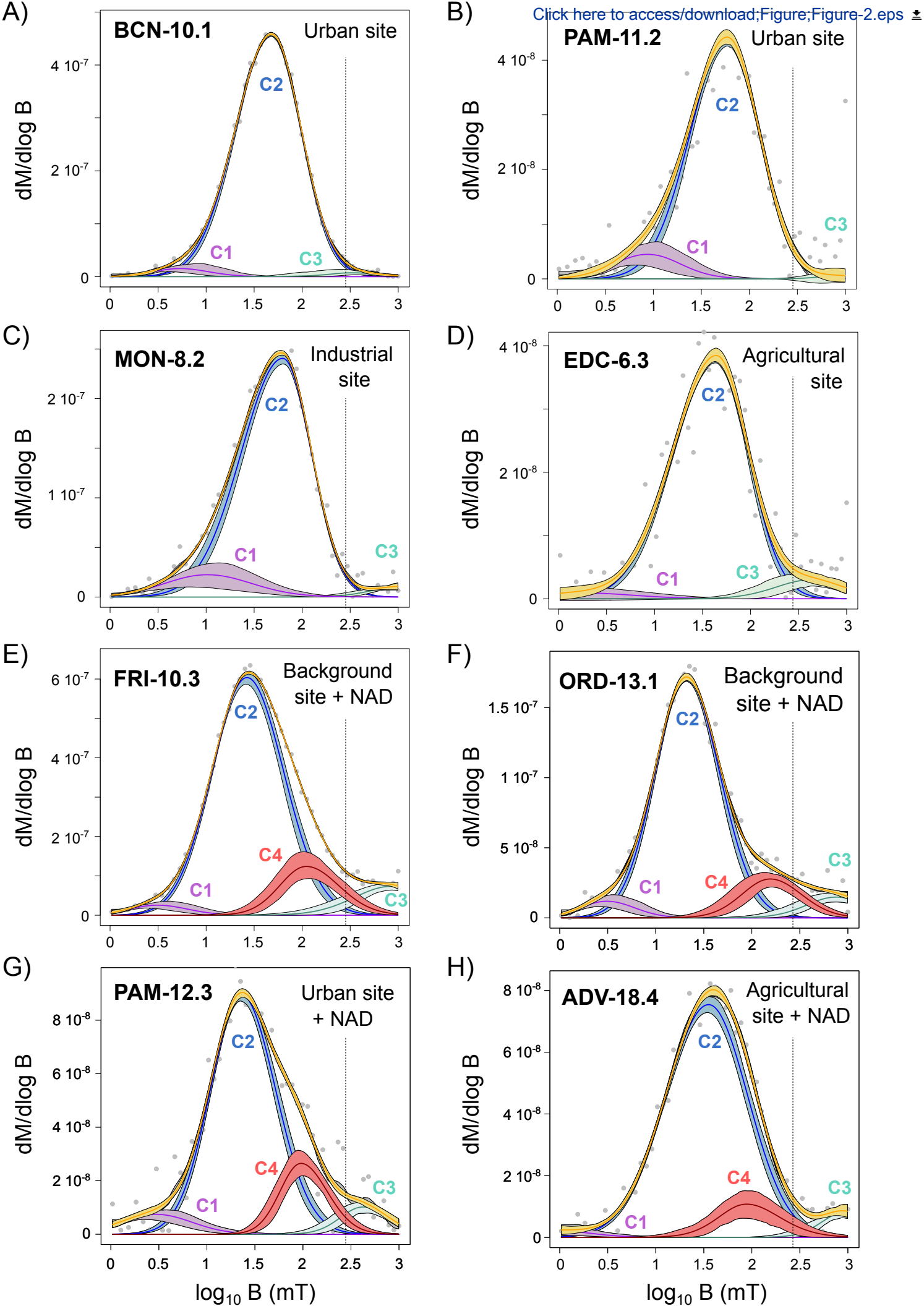

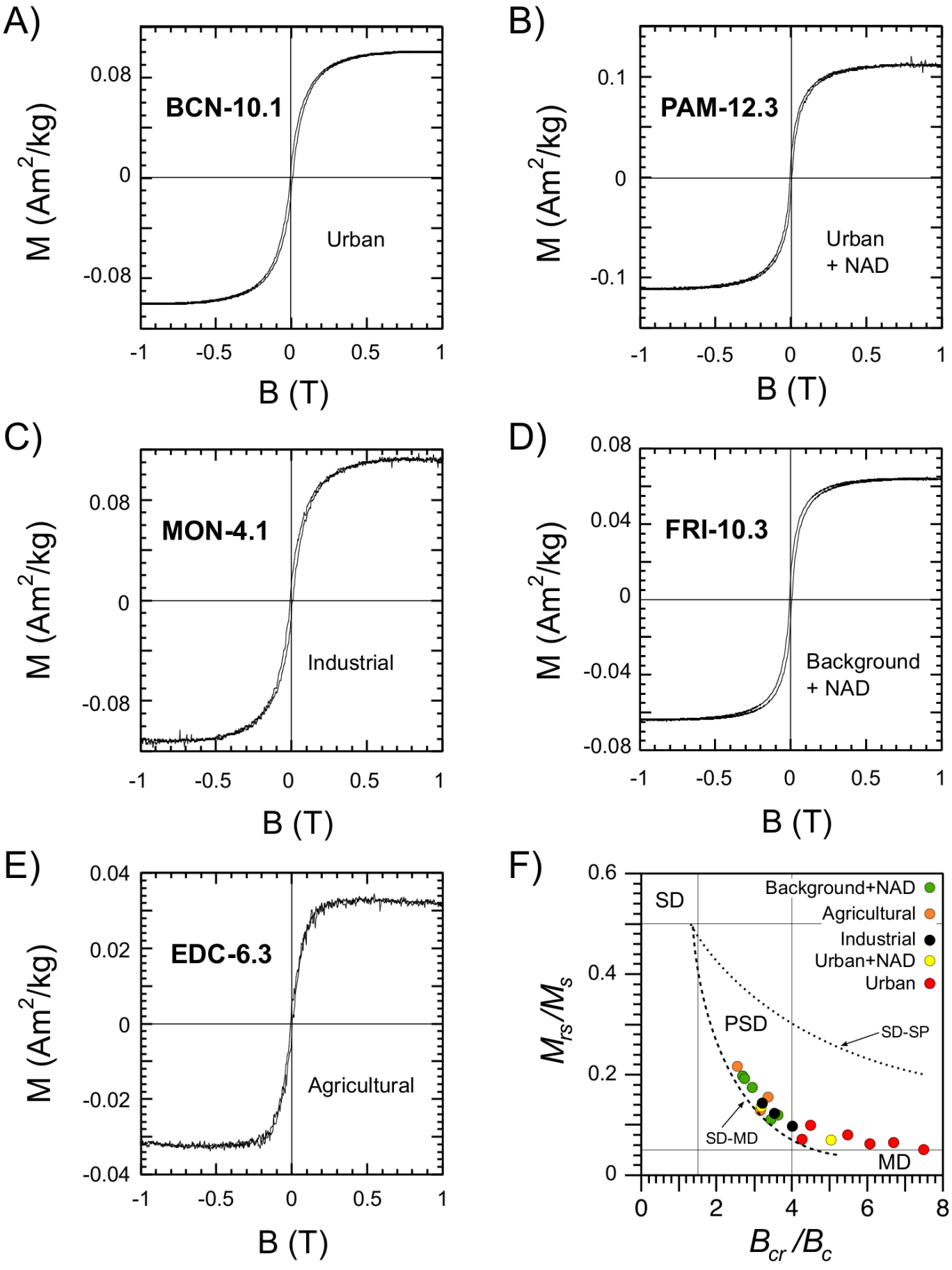

Figure 4



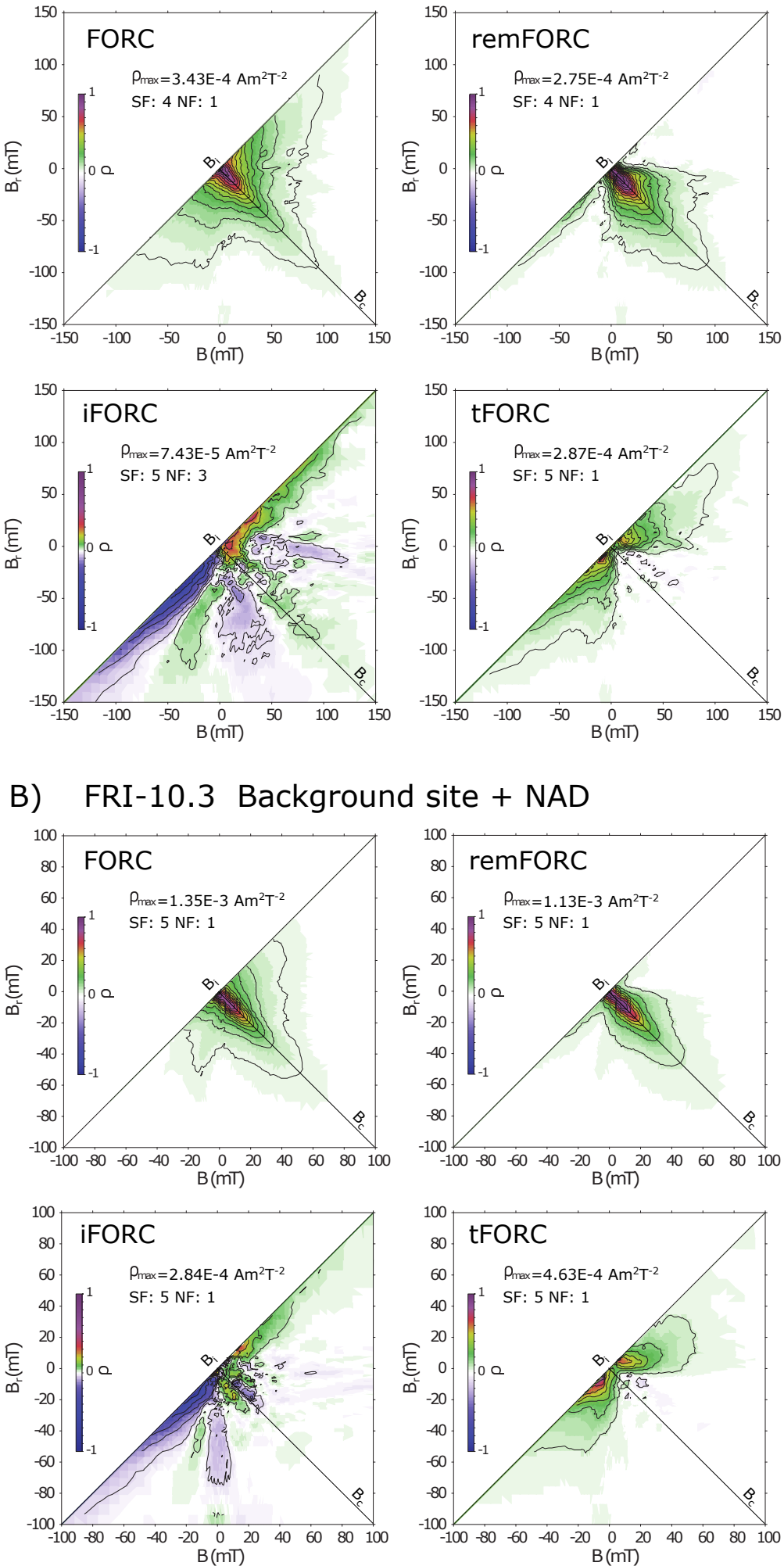

Figure 5

Click here to access/download;Figure;Figure-5.eps

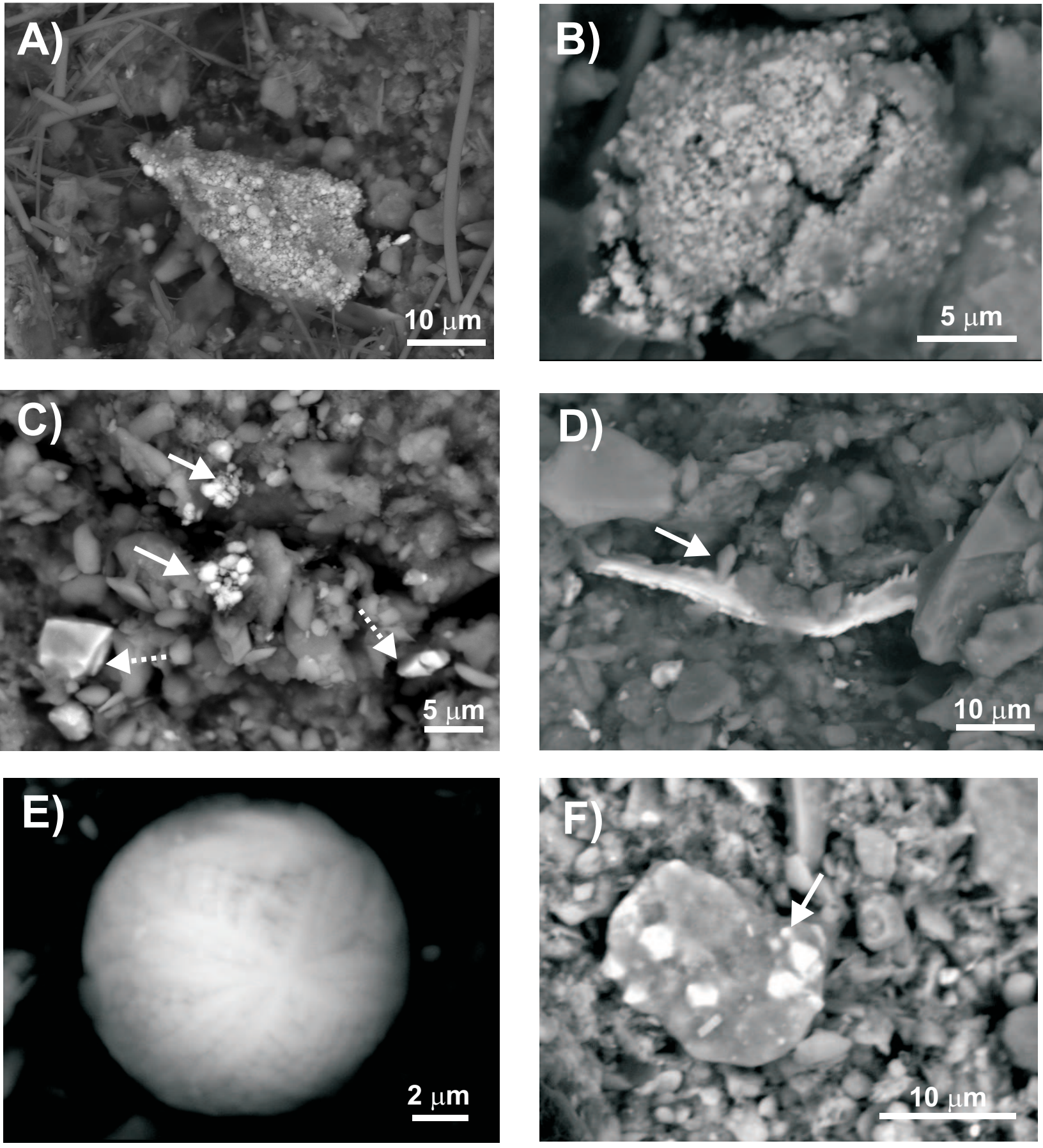

Figure 6

Click here to access/download;Figure;Figure-6.eps

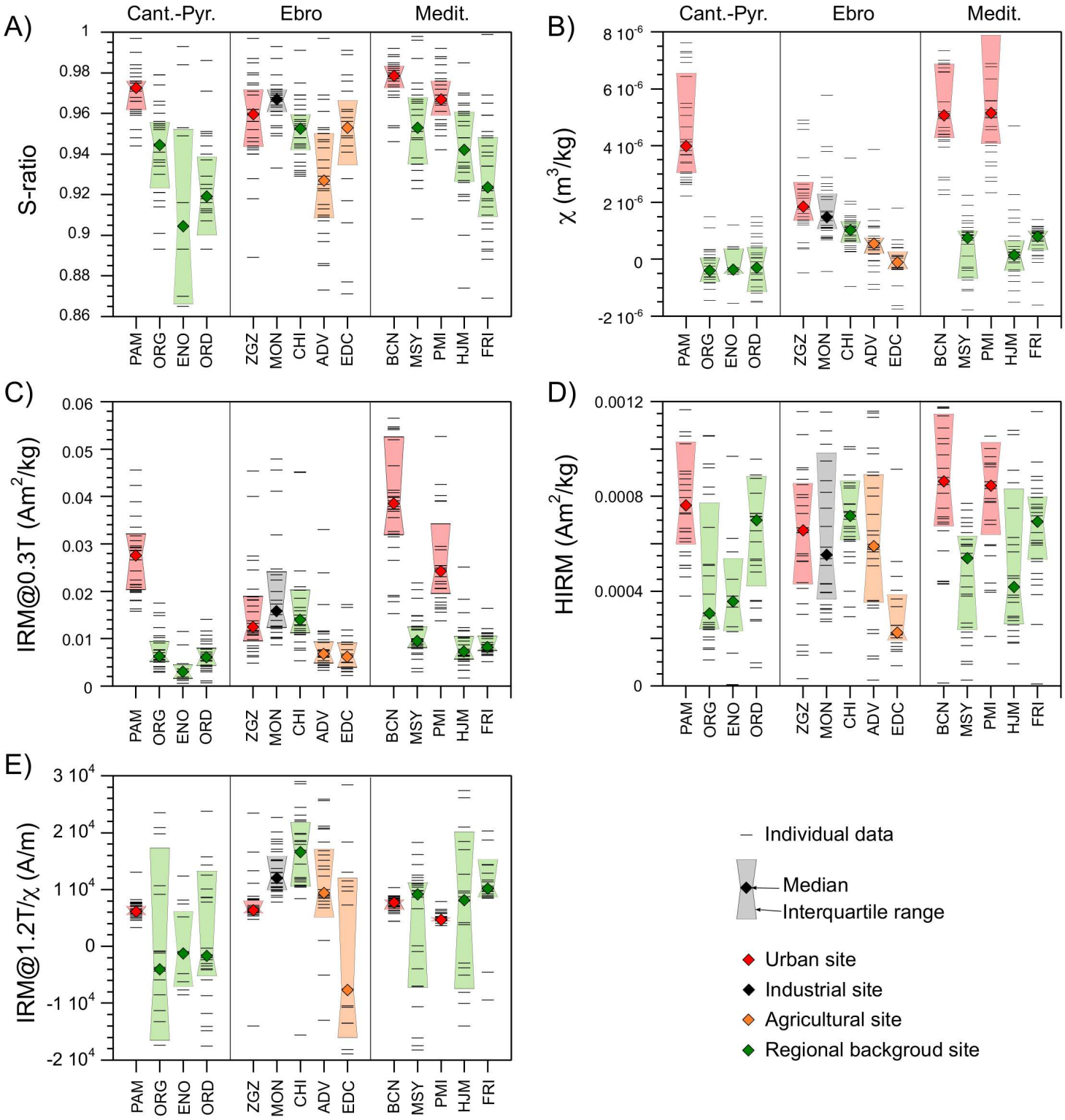

Figure 7

Click here to access/download;Figure;Figure-7.eps

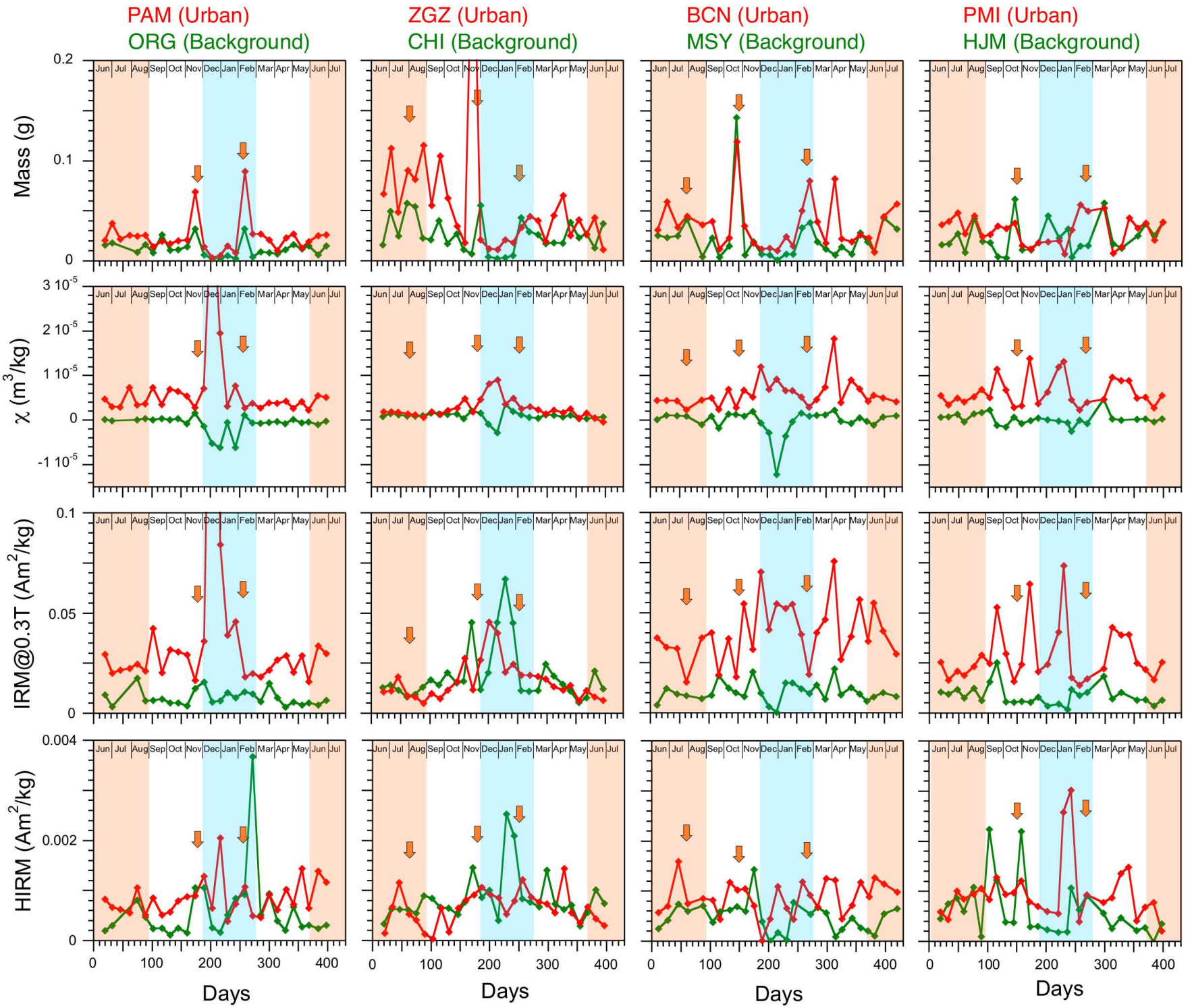

Figure 8

Click here to access/download;Figure;Figure-8.eps

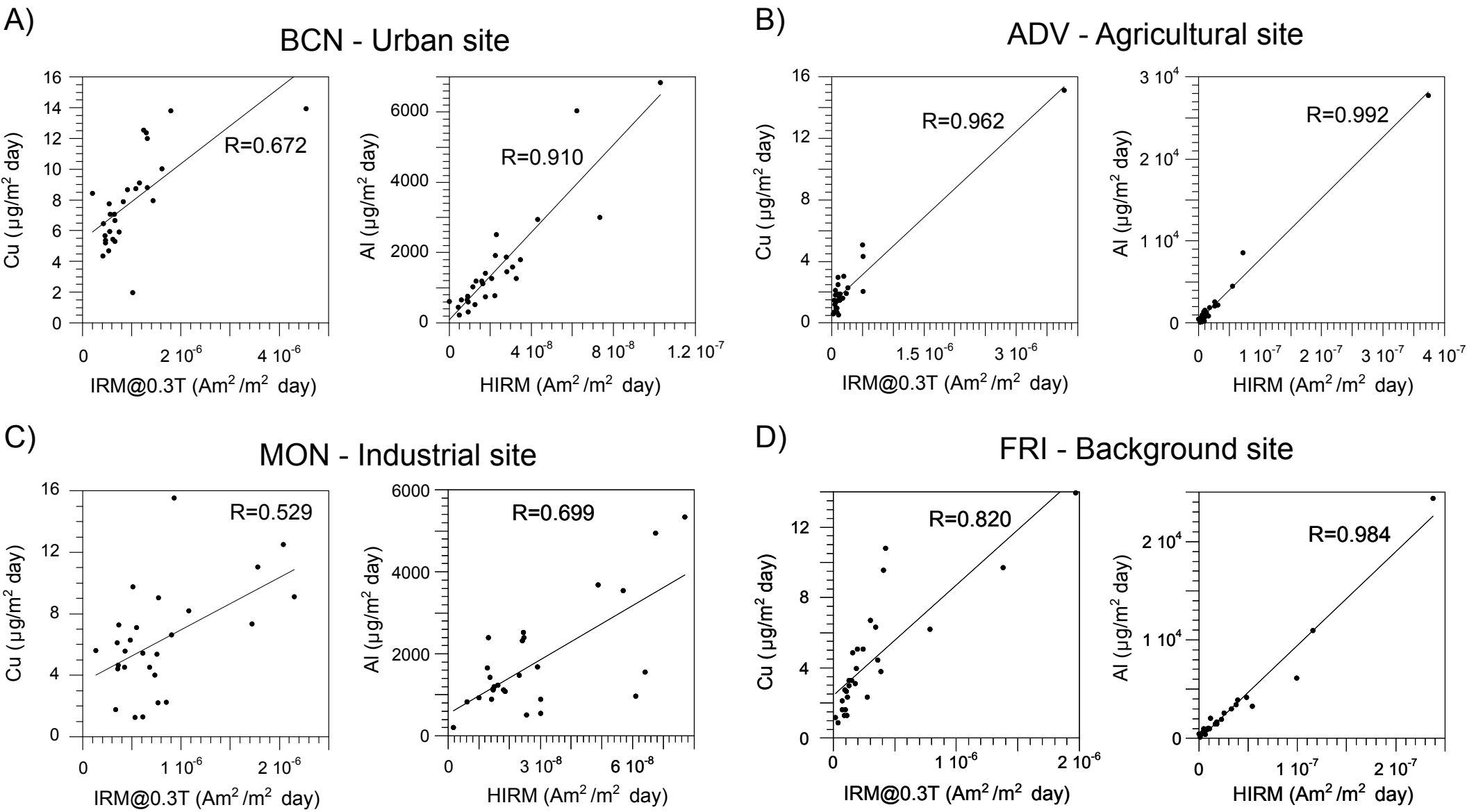

Figure 9a-b

Click here to access/download;Figure;Figure-9a-b.eps

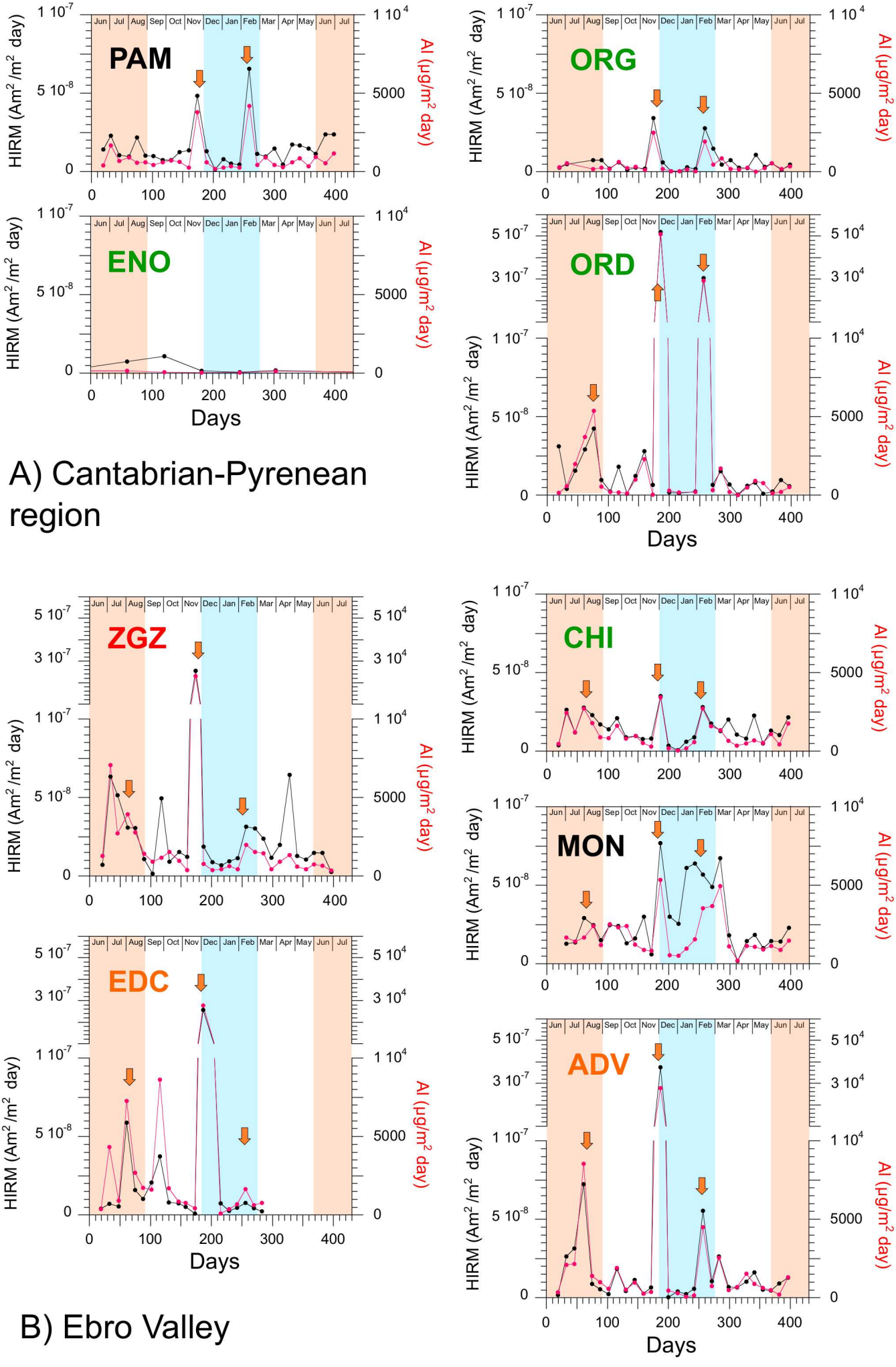

Figure 9c



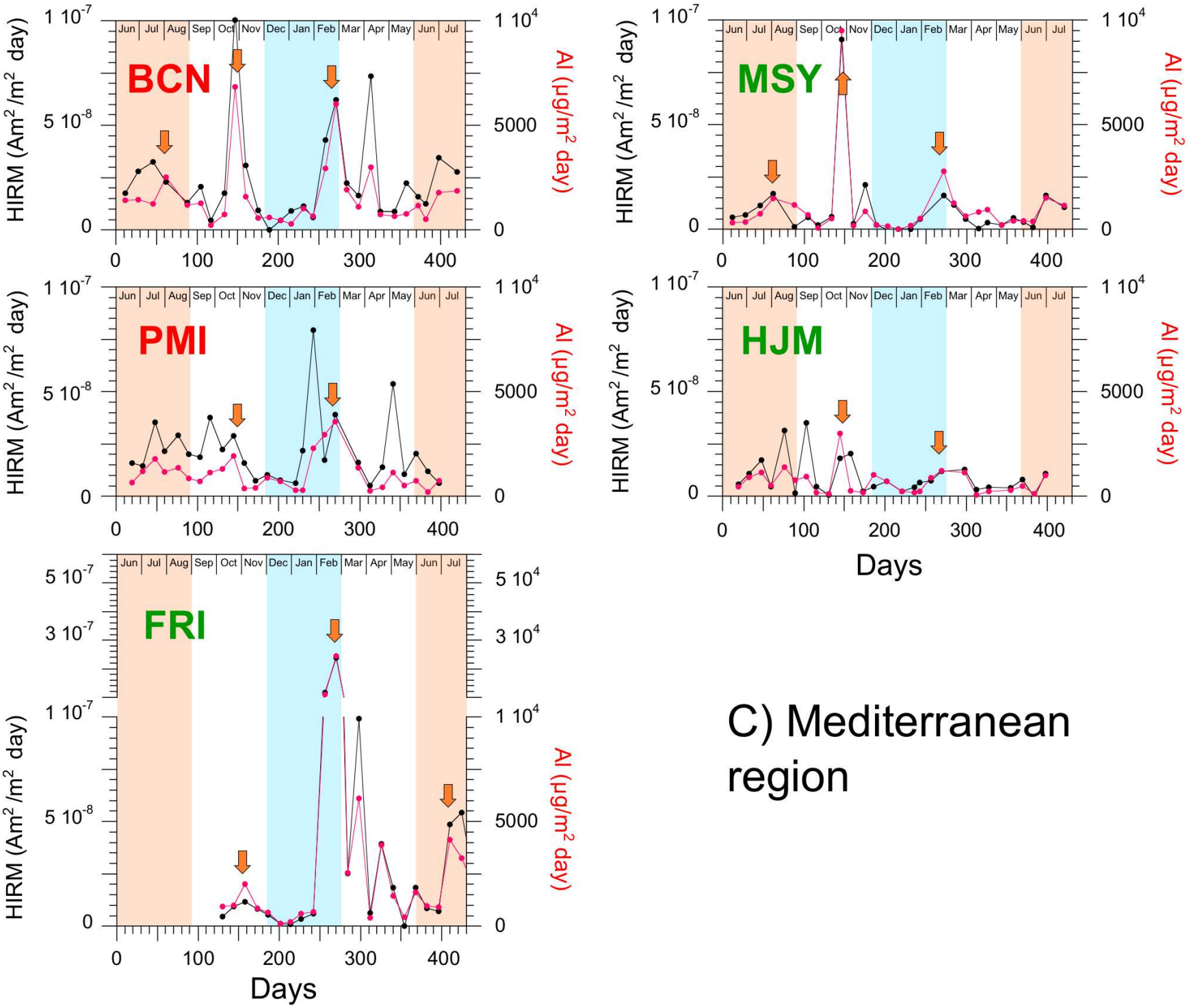

Figure 10a-b

Click here to access/download;Figure;Figure-10a-b.eps

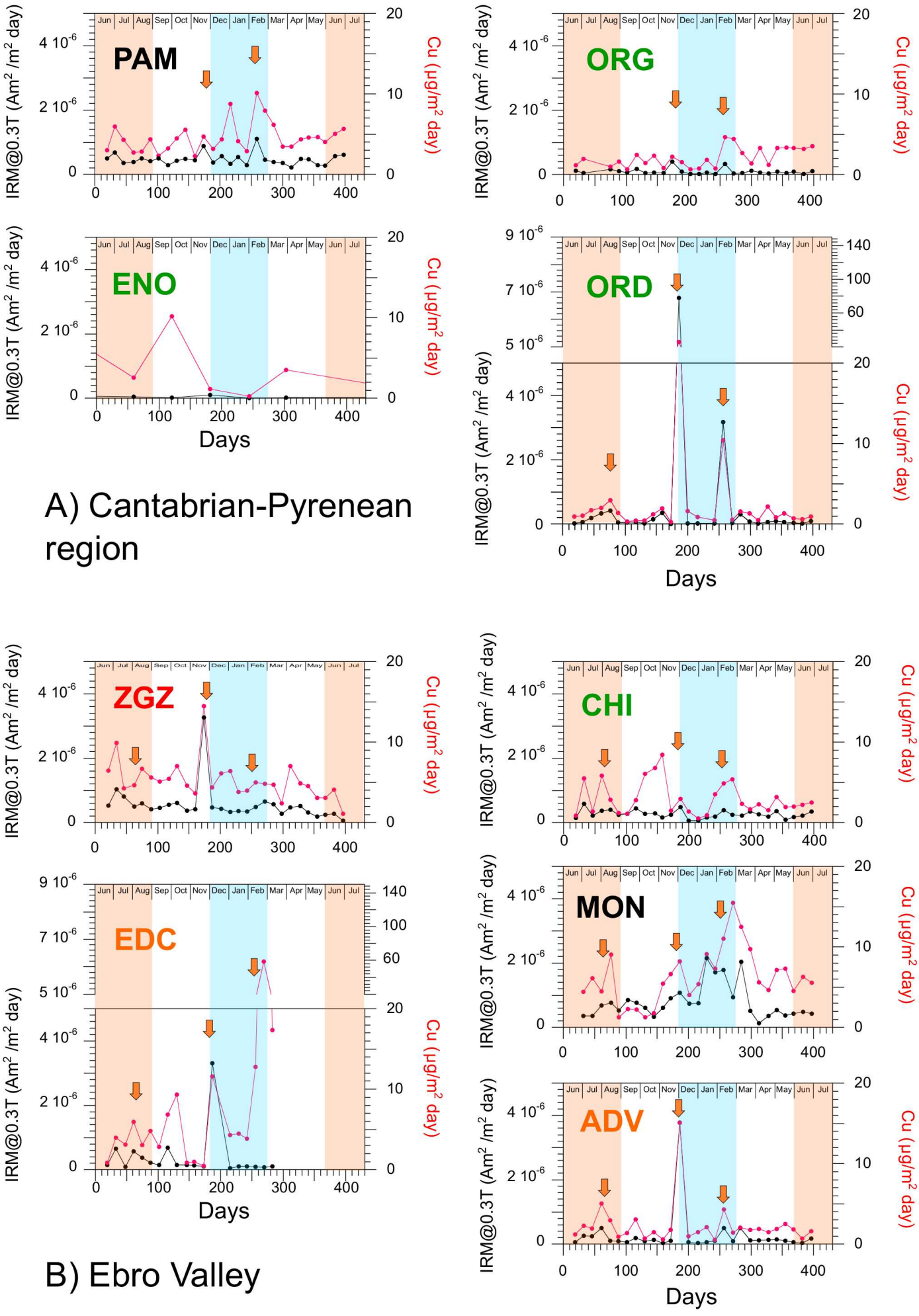

Figure 10c

Click here to access/download;Figure;Figure-10c.eps

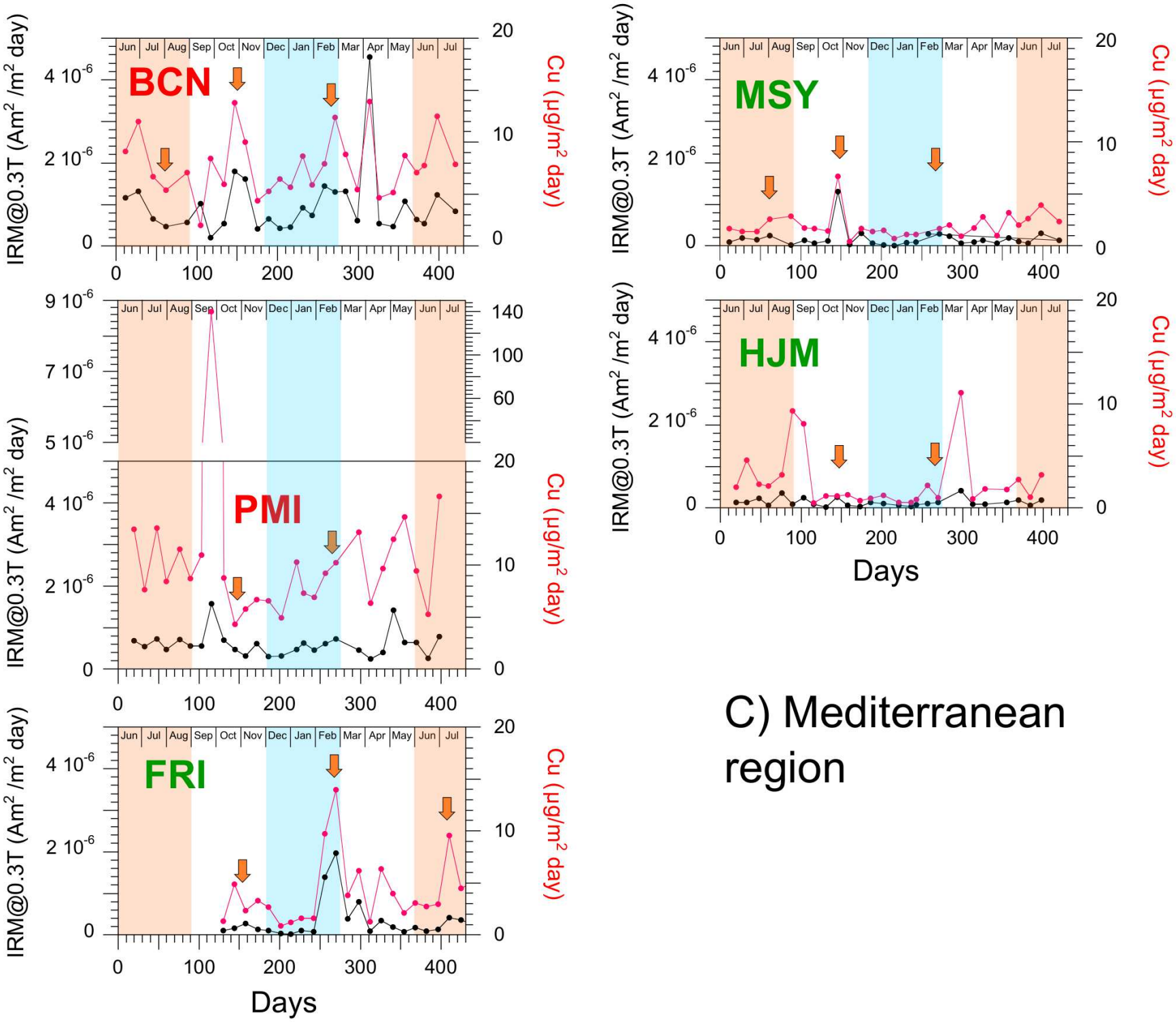

Table 1



| Site | Abbreviation | Type | Latitude | Longitude | Altitude m a. s. l. | Annual rainfall ($l/m^2$) | Start date | End date |
|---|---|---|---|---|---|---|---|---|
| ***Cantabrian and Pyrenean region*** | | | | | | | | |
| Pamplona | PAM | Urban | 42,800 | -1,650 | 450 | 711 | Jun. 2016 | Jun. 2017 |
| Orgi * | ORG | Regional background | 42,960 | -1,680 | 512 | 766 | Jun. 2016 | Jun. 2017 |
| Ordesa | ORD | Regional background | 42,650 | -0,090 | 1190 | 1119 | Jun. 2016 | Jun. 2017 |
| Enol | ENO | Regional background | 43,272 | -4,991 | 1070 | 1722 | Dec. 2015 | Jun. 2017 |
| ***Ebro Valley*** | | | | | | | | |
| Zaragoza | ZGZ | Urban | 41,640 | -0,890 | 247 | 295 | Jun. 2016 | Jun. 2017 |
| Monzón | MON | Industrial | 41,920 | 0,190 | 279 | 519 | Jun. 2016 | Jun. 2017 |
| Chiprana * | CHI | Regional background | 41,290 | -0,240 | 156 | 287 | Jun. 2016 | Jun. 2017 |
| Almudévar | ADV | Agricultural | 42,020 | -0,660 | 456 | 473 | Jun. 2016 | Jun. 2017 |
| Ejea | EDC | Agricultural | 42,060 | -1,130 | 336 | 251 | Jun. 2016 | Mar. 2017 |
| ***Mediterranean region*** | | | | | | | | |
| Barcelona | BCN | Urban | 41,390 | 2,120 | 63 | 563 | Jun. 2016 | Jun. 2017 |
| Montseny * | MSY | Regional background | 41,780 | 2,350 | 720 | 546 | Jun. 2016 | Jun. 2017 |
| Palma | PMI | Urban | 39,570 | 2,660 | 12 | 601 | Jun. 2016 | Jun. 2017 |
| Joan March * | HJM | Regional background | 39,680 | 2,690 | 172 | 544 | Jun. 2016 | Jun. 2017 |
| Frigiliana | FRI | Regional background | 36,792 | -3,898 | 320 | 506 | Oct. 2016 | Jul. 2017 |

Table 2



| Sample | Type | $B_{cr}$ (mT) | $M_r/M_s$ | $B_{cr}/B_c$ | Component 1 | | | | Component 2 | | | | Component 3 | |
|---|---|---|---|---|---|---|---|---|---|---|---|---|---|---|
| | | | | | *Bh (mT)* | *DP* | *S* | *EC* | *Bh (mT)* | *DP* | *S* | *EC* | *Bh (mT)* | *DP* |
| PAM-11.2 | Urban | 31.90 | 0.062 | 6.070 | 8.40 | 0.34 | 1.01 | 0.0885 | 53.53 | 0.36 | 0.93 | 0.9038 | 897.20 | 0.25 |
| ZGZ-10.3 | Urban | 33.58 | 0.052 | 7.490 | 9.40 | 0.33 | 1.05 | 0.0658 | 51.40 | 0.36 | 0.83 | 0.8819 | 807.12 | 0.37 |
| BCN-2.3 | Urban | 33.40 | 0.100 | 4.480 | 13.26 | 0.41 | 1.02 | 0.1101 | 51.91 | 0.37 | 0.90 | 0.8333 | 686.46 | 0.30 |
| BCN-10.1 | Urban | 28.56 | 0.072 | 4.270 | 5.39 | 0.27 | 1.03 | 0.0270 | 42.45 | 0.34 | 0.91 | 0.9604 | 359.55 | 0.13 |
| PMI-2.3 | Urban | 27.77 | 0.080 | 5.470 | 12.71 | 0.40 | 1.05 | 0.1755 | 51.82 | 0.37 | 0.90 | 0.7874 | 1338.26 | 0.29 |
| PMI-8.3 | Urban | 30.89 | 0.066 | 6.700 | 9.34 | 0.34 | 0.93 | 0.1145 | 51.80 | 0.36 | 0.82 | 0.8763 | 493.02 | 0.25 |
| MON-4.1 | Industrial | 32.14 | 0.122 | 3.540 | - | - | - | - | 41.44 | 0.42 | 0.83 | 0.9544 | 860.60 | 0.30 |
| MON-8.2 | Industrial | 32.20 | 0.096 | 4.010 | 10.50 | 0.46 | 1.05 | 0.1000 | 49.09 | 0.37 | 0.83 | 0.8661 | 1101.13 | 0.33 |
| MON-13.1 | Industrial | 24.82 | 0.142 | 3.210 | 2.31 | 0.41 | 1.07 | 0.0190 | 36.84 | 0.44 | 0.99 | 0.9465 | 791.32 | 0.26 |
| EDC-6.3 | Agricultural | 25.68 | 0.155 | 3.360 | 0.50 | 0.50 | 1.05 | 0.0204 | 35.22 | 0.39 | 0.86 | 0.9125 | 422.44 | 0.36 |
| PAM-12.3 | Urban + NAD | 20.00 | 0.136 | 3.180 | 2.90 | 0.37 | 1.00 | 0.0592 | 24.26 | 0.34 | 1.05 | 0.7230 | 450.76 | 0.26 |
| ZGZ-18.1 | Urban + NAD | 28.75 | 0.070 | 5.030 | 3.16 | 0.45 | 1.12 | 0.0278 | 42.52 | 0.40 | 0.88 | 0.9241 | 951.25 | 0.35 |
| ORD-5.3 | Background + NAD | 28.25 | 0.111 | 3.420 | 5.31 | 0.16 | 1.03 | 0.0244 | 34.82 | 0.38 | 1.02 | 0.7801 | 588.86 | 0.28 |
| ORD-13.1 | Background + NAD | 17.86 | 0.197 | 2.670 | 3.15 | 0.27 | 1.04 | 0.0434 | 21.63 | 0.34 | 1.03 | 0.7740 | 795.11 | 0.33 |
| ORD-18.1 | Background + NAD | 18.44 | 0.192 | 2.720 | 3.14 | 0.33 | 0.89 | 0.0474 | 22.57 | 0.33 | 1.03 | 0.7596 | 580.01 | 0.28 |
| HJM-19.1 | Background + NAD | 26.56 | 0.120 | 3.600 | 2.82 | 0.18 | 1.03 | 0.0303 | 32.61 | 0.36 | 1.02 | 0.7665 | 547.26 | 0.28 |
| FRI-10.3 | Background + NAD | 22.83 | 0.175 | 2.930 | 3.19 | 0.30 | 1.05 | 0.0249 | 27.52 | 0.37 | 1.03 | 0.7559 | 736.59 | 0.36 |
| ADV-8.4 | Agricultural + NAD | 26.49 | 0.129 | 3.160 | 1.04 | 0.33 | 1.13 | 0.0096 | 32.97 | 0.43 | 0.95 | 0.8406 | 1023.08 | 0.27 |
| ADV-13.1 | Agricultural + NAD | 17.82 | 0.217 | 2.560 | 2.37 | 0.23 | 1.03 | 0.0264 | 19.20 | 0.34 | 0.93 | 0.7026 | 666.47 | 0.37 |

| | | Component 4 | | | |
|---|---|---|---|---|---|
| ***S*** | ***EC*** | ***Bh (mT)*** | ***DP*** | ***S*** | ***EC*** |
| 1.11 | 0.0077 | - | - | - | - |
| 1.10 | 0.0523 | - | - | - | - |
| 1.14 | 0.0565 | - | - | - | - |
| 1.15 | 0.0127 | - | - | - | - |
| 1.13 | 0.0371 | - | - | - | - |
| 1.19 | 0.0092 | - | - | - | - |
| 1.14 | 0.0456 | - | - | - | - |
| 1.06 | 0.0339 | - | - | - | - |
| 1.28 | 0.0345 | - | - | - | - |
| 1.03 | 0.0671 | - | - | - | - |
| 1.08 | 0.0624 | 105.81 | 0.25 | 1.13 | 0.0624 |
| 1.11 | 0.0481 | - | - | - | - |
| 0.98 | 0.0737 | 128.19 | 0.30 | 1.30 | 0.0737 |
| 1.05 | 0.0662 | 165.20 | 0.31 | 1.07 | 0.0662 |
| 1.06 | 0.0611 | 149.61 | 0.29 | 1.16 | 0.0611 |
| 1.01 | 0.0824 | 120.98 | 0.29 | 1.00 | 0.0824 |
| 0.89 | 0.0886 | 124.09 | 0.31 | 1.11 | 0.0886 |
| 1.11 | 0.0582 | 97.85 | 0.33 | 1.12 | 0.0582 |
| 1.14 | 0.0783 | 99.49 | 0.36 | 1.09 | 0.0783 |

Table 3



| Site | IRM@0.3T Vs Cu | IRM@0.3T Vs Sb | HIRM Vs Al | HIRM Vs Ti |
|---|---|---|---|---|
| PAM | 0.47 | 0.44 | 0.31 | 0.26 |
| ORG | 0.27 | 0.45 | **0.89** | **0.79** |
| ORD | **0.99** | **0.99** | **0.99** | **0.97** |
| ENO | 0.19 | 0.02 | 0.45 | 0.06 |
| ZGZ | **0.85** | 0.29 | **0.96** | **0.88** |
| MON | 0.52 | 0.61 | 0.66 | 0.62 |
| CHI | 0.34 | 0.19 | **0.89** | **0.81** |
| ADV | **0.96** | 0.31 | **0.99** | **0.85** |
| EDC | 0.01 | 0.4 | **0.97** | **0.83** |
| BCN | 0.67 | 0.69 | **0.91** | **0.95** |
| MSY | **0.81** | **0.92** | **0.96** | **0.97** |
| PMI | 0.69 | **0.72** | 0.57 | 0.44 |
| HJM | 0.59 | 0.65 | 0.54 | 0.5 |
| FRI | **0.82** | 0.21 | **0.98** | **0.96** |

Click here to access/download

**Supplementary Material**

Supplementary Table 1.xlsx

We wish to confirm that there are no known conflicts of interest associated with this publication and there has been no significant financial support for this work that could have influenced its outcome.